

# Excited state baryon spectroscopy from lattice QCD

Robert G. Edwards,<sup>1,\*</sup> Jozef J. Dudek,<sup>1,2,†</sup> David G. Richards,<sup>1,‡</sup> and Stephen J. Wallace<sup>3,§</sup>  
(for the Hadron Spectrum Collaboration)

<sup>1</sup>Jefferson Laboratory, 12000 Jefferson Avenue, Newport News, VA 23606, USA

<sup>2</sup>Department of Physics, Old Dominion University, Norfolk, VA 23529, USA

<sup>3</sup>Department of Physics, University of Maryland, College Park, MD 20742, USA  
(Dated: June 6, 2011)

We present a calculation of the Nucleon and Delta excited state spectrum on dynamical anisotropic clover lattices. A method for operator construction is introduced that allows for the reliable identification of the continuum spins of baryon states, overcoming the reduced symmetry of the cubic lattice. Using this method, we are able to determine a spectrum of single-particle states for spins up to and including  $J = \frac{7}{2}$ , of both parities, the first time this has been achieved in a lattice calculation. We find a spectrum of states identifiable as admixtures of  $SU(6) \otimes O(3)$  representations and a counting of levels that is consistent with the non-relativistic  $qqq$  constituent quark model. This dense spectrum is incompatible with quark-diquark model solutions to the “missing resonance problem” and shows no signs of parity doubling of states.

## I. INTRODUCTION

Explaining the excitation spectrum of baryons is core to our understanding of QCD in the low-energy regime, and if we truly understand QCD in the strong-coupling regime, we should be able to confront experimental spectroscopic data with first-principles calculations within QCD. The experimental investigation of the excited baryon spectrum has been a long-standing element of the hadronic-physics program. An important goal has been the search for so-called “missing resonances”, baryonic states predicted by the quark model based on three constituent quarks but which have not yet been observed experimentally; should such states not be found, it may indicate that the baryon spectrum can be modeled with fewer effective degrees of freedom, such as in quark-diquark models. In the past decade, there has been an extensive program to collect data on electromagnetic production of one and two mesons at Jefferson Lab, MIT-Bates, LEGS, MAMI, ELSA, and GRAAL. To analyse these data, and thereby refine our knowledge of the baryon spectrum, a variety of physics analysis models have been developed at Bonn, George Washington University, Jefferson Laboratory and Mainz.

The experimental efforts outlined above should be complemented by high-quality *ab initio* computations within lattice QCD. Historically, the calculation of the masses of the lowest-lying states, for both baryons and mesons, has been a benchmark calculation of this discretized, finite-volume computational approach, where the aim is well-understood control over the various systematic errors that enter into a calculation; for a recent review, see [1]. However, there is now increasing effort

aimed at calculating the excited states of the theory, with several groups presenting investigations of the low-lying excited baryon spectrum, using a variety of discretizations, numbers of quark flavors, interpolating operators, and fitting methodologies [2–5]. Some aspects of these calculations remain unresolved and are the subject of intense effort, notably the ordering of the Roper resonance in the low-lying Nucleon spectrum.

A basis of baryon operators for states at rest, respecting the (cubic) symmetry of the lattice, was developed in Refs. [6, 7], and subsequently used in calculations of the excited state Nucleon spectrum in both quenched QCD[8], and with two dynamical quark flavors[9]. In parallel, we studied Clover fermions on anisotropic lattices[10, 11], with a finer temporal than spatial resolution, enabling the hadron correlation functions to be observed at short temporal distances and hence many energy levels to be extracted. Crucial to our determination of the spectrum has been the use of the variational method [12–14] with a large number of interpolating operators at both the source and the sink; we developed and used the “distillation” method, enabling the necessary correlation functions to be computed in an efficient manner. A recent calculation of the Nucleon,  $\Delta$  and  $\Omega$  excited-state spectrum demonstrated the efficacy of the method[15].

In this paper, we expand the above program of computations considerably, extending to baryons the spin-identification techniques developed for mesons in Refs. [16, 17]. We develop a new basis of interpolating operators with good total angular momentum,  $J$ , in the continuum, which are then subduced to the various lattice irreducible representations (irreps). We find that the subduced operators retain a memory of their continuum antecedents to a remarkable degree. For example, hadron correlation functions between operators subduced from different continuum spins  $J$  are suppressed relative to those subduced from the same  $J$ , illustrating an approximate realization of rotational symmetry at the scale

\*Electronic address: edwards@jlab.org

†Electronic address: dudek@jlab.org

‡Electronic address: dgr@jlab.org

§Electronic address: stevewal@umd.edu

$\frac{a_t m_\ell}{a_t m_s}$	$\frac{m_\pi}{\text{MeV}}$	$m_K/m_\pi$	$a_t m_\Omega$	volume	$N_{\text{cfigs}}$	$N_{\text{tsrcs}}$	$N_{\text{vecs}}$
$\frac{-0.0808}{-0.0743}$	524	1.15	0.3200(7)	$16^3 \times 128$	500	7	56
$\frac{-0.0830}{-0.0743}$	444	1.29	0.3040(8)	$16^3 \times 128$	601	5	56
$\frac{-0.0840}{-0.0743}$	396	1.39	0.2951(22)	$16^3 \times 128$	479	8	56

TABLE I: The lattice data sets and propagators used in this paper. The light and strange quark mass as well as the  $\Omega$  baryon mass in temporal lattice units are shown. The pion mass, lattice size and number of configurations are listed, as well as the number of time-sources and the number of distillation vectors  $N_{\text{vecs}}$ .

of hadrons. This allows us to determine reliably the spins of most of the (single-particle) states, which helps to delineate between the nearly degenerate energy levels we observe in the spectrum. We are thereby able to determine the highly excited spectrum, including spins up to  $J = \frac{7}{2}$ , and to resolve the masses of the low-lying states with a statistical precision at or below 1%.

The remainder of the paper is organized as follows. In Section II we describe the parameters of the lattice gauge fields used in our calculation. The “distillation” method, and its application to the construction of baryon correlation functions is outlined in Section III. Section IV describes the procedure for constructing baryon interpolating operators with good continuum spin. Angular dependence transforming like orbital angular momenta is incorporated through covariant derivatives that transform as representations with  $L = 1$  and  $L = 2$ ; a detailed construction is provided in Appendix A. We also develop subduction matrices that allow the continuum operators to be subduced to irreducible representations of the cubic group; a derivation for half-integer spins up to  $\frac{9}{2}$  is given in Appendix B, where tables of the subduction matrices are also given. Our implementation of the variational method is presented in Section V, and our procedure for determining the spins of the resulting lattice states is described in Section VI, which also shows tests of the approximate rotational invariance in the spectra. The stability of the resultant spectra with respect to changes in the analysis method is discussed in Section VII. We present our results in Section VIII, beginning with a detailed discussion of the spectrum at the heaviest of our quark masses before examining the quark mass dependence. Discussion of multi-particle states is given in Section IX. We summarize our findings and provide our conclusions in Section X.

## II. GAUGE FIELDS

A major challenge in the extraction of the spectrum of excited states from a lattice calculation is that the correlation functions, or more specifically the principal correlators of the variational method that correspond to excited states, decay increasingly rapidly with Euclidean time as the energy of the state increases, whilst the noise behaves in the same manner as in the ground

state. Hence the signal-to-noise ratio for excited-state correlators exhibits increasingly rapid degradation with Euclidean time with increasing energy. To ameliorate this problem we have adopted a dynamical anisotropic lattice formulation whereby the temporal extent is discretized with a finer lattice spacing than in the spatial directions; this approach avoids the computational cost that would come from reducing the spacing in all directions, and is core to our excited-state spectroscopy program. Improved gauge and fermion actions are used, with two mass-degenerate light dynamical quarks and one strange dynamical quark, of masses  $m_l$  and  $m_s$  respectively. Details of the formulation of the actions as well as the techniques used to determine the anisotropy parameters can be found in Refs. [10, 11].

The lattices have a spatial lattice spacing  $a_s \sim 0.123$  fm with a temporal lattice spacing approximately 3.5 times smaller, corresponding to a temporal scale  $a_t^{-1} \sim 5.6$  GeV. In this work, results are presented for the light quark baryon spectrum at quark mass parameters  $a_t m_l = (-0.0808, -0.0830, -0.0840)$  and  $a_t m_s = -0.0743$ , and lattice sizes of  $16^3 \times 128$  with spatial extent  $\sim 2$  fm. The bare strange quark mass is held fixed to its tuned value of  $a_t m_s = -0.0743$ ; some details of the lattices are provided in Table I. The lattice scale, as quoted above, is determined by an extrapolation to the physical quark mass limit using the  $\Omega$  baryon mass (denoted by  $a_t m_\Omega$ ). To facilitate comparisons of the spectrum at different quark masses, the ratio of hadron masses with the  $\Omega$  baryon mass obtained on the same ensemble is used to remove the explicit scale dependence, following Ref. [11].

## III. CORRELATOR CONSTRUCTION USING DISTILLATION

The determination of the excited baryon spectrum proceeds through the calculation of matrices of correlation functions between baryon creation and annihilation operators at time 0 and  $t$  respectively:

$$C_{ij}(t) = \langle 0 | \mathcal{O}_i(t) \mathcal{O}_j^\dagger(0) | 0 \rangle.$$

Inserting a complete set of eigenstates of the Hamiltonian, we have

$$C_{ij}(t) = \sum_{\mathbf{n}} \frac{1}{2E_{\mathbf{n}}} \langle 0 | \mathcal{O}_i | \mathbf{n} \rangle \langle \mathbf{n} | \mathcal{O}_j^\dagger | 0 \rangle e^{-E_{\mathbf{n}} t}, \quad (1)$$

where the sum is over all states that have the same quantum numbers as the interpolating operators  $\{\mathcal{O}_i\}$ . Note that in a finite volume, this yields a discrete set of energies.

Smearing is a well-established means of suppressing the short-distance modes that do not contribute significantly to the low-energy part of the spectrum, and in turn, allows for the construction of operators that couple predominantly to the low-lying states. A widely

adopted version is Jacobi smearing, which uses the three-dimensional Laplacian,

$$-\nabla_{xy}^2(t) = 6\delta_{xy} - \sum_{j=1}^3 \left( \tilde{U}_j(x, t)\delta_{x+\hat{j}, y} + \tilde{U}_j^\dagger(x - \hat{j}, t)\delta_{x-\hat{j}, y} \right),$$

where the gauge fields,  $\tilde{U}$  may be constructed from an appropriate covariant gauge-field-smearing algorithm [18]. From this a simple smearing operator,

$$J_{\sigma, n_\sigma}(t) = \left( 1 + \frac{\sigma \nabla^2(t)}{n_\sigma} \right)^{n_\sigma},$$

is subsequently applied to the quark fields  $\psi$ ; for large  $n_\sigma$ , this approaches a Gaussian form  $\exp \sigma \nabla^2(t)$ . “Distillation”[19], the method we adopt, replaces the smearing function by an outer product over the low-lying eigenmodes of the Laplacian,

$$\square_{xy}(t) = \sum_{k=1}^N \xi_x^{(k)}(t) \xi_y^{(k)\dagger}(t), \quad (2)$$

where the  $\xi^{(k)}(t)$  is the  $k^{\text{th}}$  eigenvector of  $\nabla_{xy}^2(t)$ , ordered by the magnitude of the eigenvalue; the (volume-dependent) number of modes  $N$  should be sufficient to sample the required angular structure at the hadronic scale[17, 19], but is small compared to the number of sites on a time slice. Thus distillation is a highly efficient way of computing hadron correlation functions.

To illustrate how distillation is applied to the construction of the baryon correlators, we specialize to the case of a positively charged isospin- $\frac{1}{2}$  baryon. A generic annihilation operator can be written

$$\mathcal{O}_i(t) = \epsilon^{abc} S_{\alpha\beta\gamma}^i (\mathbf{\Gamma}_1 \square d)_\alpha^a (\mathbf{\Gamma}_2 \square u)_\beta^b (\mathbf{\Gamma}_3 \square u)_\gamma^c(t), \quad (3)$$

where  $u$  and  $d$  are  $u$ - and  $d$ -quark fields respectively,  $\mathbf{\Gamma}_j$  is a spatial operator, including possible displacements, acting on quark  $j$ ,  $a, b, c$  are color indices, and  $\alpha, \beta, \gamma$  are spin indices;  $S$  encodes the spin structure of the operator, and is constructed so that the operator has the desired quantum numbers, as discussed in the next section. We now construct a baryon correlation function as

$$C_{ij}(t) = \epsilon^{abc} \epsilon^{\bar{a}\bar{b}\bar{c}} S_{\alpha\beta\gamma}^i \bar{S}_{\bar{\alpha}\bar{\beta}\bar{\gamma}}^{*j} \times \left\langle [(\mathbf{\Gamma}_1 \square d)_\alpha^a (\mathbf{\Gamma}_2 \square u)_\beta^b (\mathbf{\Gamma}_3 \square u)_\gamma^c(t)] \cdot [(\bar{d} \square \bar{\mathbf{\Gamma}}_1)_{\bar{\alpha}}^{\bar{a}} (\bar{u} \square \bar{\mathbf{\Gamma}}_2)_{\bar{\beta}}^{\bar{b}} (\bar{u} \square \bar{\mathbf{\Gamma}}_3)_{\bar{\gamma}}^{\bar{c}}(0)] \right\rangle,$$

where the bar over  $S$  and  $\mathbf{\Gamma}$  indicate these belong to the creation operator. Inserting the outer-product decomposition of  $\square$  from Eq. 2, we can express the correlation function as

$$C_{ij}(t) = \Phi_{\alpha\beta\gamma}^{i, (p, q, r)}(t) \Phi_{\bar{\alpha}\bar{\beta}\bar{\gamma}}^{j, (\bar{p}, \bar{q}, \bar{r})\dagger}(0) \times \left[ \tau_{\alpha\bar{\alpha}}^{p\bar{p}}(t, 0) \tau_{\beta\bar{\beta}}^{q\bar{q}}(t, 0) \tau_{\gamma\bar{\gamma}}^{r\bar{r}}(t, 0) - \tau_{\alpha\bar{\alpha}}^{p\bar{p}}(t, 0) \tau_{\beta\bar{\gamma}}^{q\bar{r}}(t, 0) \tau_{\gamma\bar{\beta}}^{r\bar{q}}(t, 0) \right], \quad (4)$$

where

$$\Phi_{\alpha\beta\gamma}^{i, (p, q, r)} = \epsilon^{abc} S_{\alpha\beta\gamma}^i (\mathbf{\Gamma}_1 \xi^{(p)})^a (\mathbf{\Gamma}_2 \xi^{(q)})^b (\mathbf{\Gamma}_3 \xi^{(r)})^c$$

encodes the choice of operator and

$$\tau_{\alpha\bar{\alpha}}^{p\bar{p}}(t, 0) = \xi^{\dagger(p)}(t) M_{\alpha\bar{\alpha}}^{-1}(t, 0) \xi^{(\bar{p})}(0)$$

is the operator-independent “perambulator”, with  $p, \bar{p}$  the eigenvector indices, and  $M$  the usual discretized Dirac operator. The perambulators play the role of the quark propagators between smeared sources and sinks. Once the perambulators have been computed, the factorization exhibited in Eq. (4) enables the correlators to be computed between any operators expressed through  $\Phi^i, \Phi^j$ , including those with displaced quark fields, at both the source and the sink. This feature will be key to our use of the variational method and the subsequent extraction of a spin-identified baryon spectrum.

#### IV. CONSTRUCTION OF BARYON OPERATORS

The construction of a comprehensive basis of baryon interpolation operators is critical to the successful application of the variational method. The lowest-lying states in the spectrum can be captured with color-singlet local baryon operators, of the form given in Eq. (3)<sup>1</sup>. Combinations of such fields can be formed so as to have definite quantum numbers, including definite symmetry properties on the cubic lattice. The introduction of a rotationally symmetric smearing operation, be it Jacobi smearing or distillation, in which the quark fields  $\psi(x)$  are replaced by quasi-local, smeared fields  $\square\psi(x)$ , does not change the symmetry properties of the interpolating operators. However, such local and quasi-local operators can only provide access to states with spins up to  $\frac{3}{2}$ . In order to access higher spins in the spectrum, and to have a sufficient basis of operators to effectively apply the variational method, it is necessary to employ non-local operators.

A basis of baryon interpolating operators incorporating angular structure, respecting the cubic symmetry of the lattice, and able to access higher spins in the spectrum, was constructed in refs. [6, 7], and these operators were employed in our earlier determinations of the spectrum. The identification of the continuum spins corresponding to the calculated energy levels remained challenging, however. To overcome this challenge, we adopt a different procedure for operator construction: we first derive a basis of operators in the continuum, with well-defined continuum spin quantum numbers, and then form the subduction of those operators into the irreducible representations of the octahedral group of the lattice.

<sup>1</sup> With, in this case,  $\mathbf{\Gamma}$  being just ordinary Dirac gamma matrices.

### A. Continuum baryon interpolating operators

Baryons are color-singlet objects, and thus they involve totally anti-symmetric combinations of the color indices of the three valence quarks. Furthermore baryon interpolating operators have to be anti-symmetric under the exchange of any pair of quarks, which is automatically satisfied since they are constructed from anti-commuting Grassmann fields. Thus the remaining quark labels, namely those of flavor, spin and spatial structure, have to be in totally symmetric combinations.

We will construct our baryon interpolating operators from products of three quark fields. Before proceeding to classify our operators, we note that three objects  $\{x, y, z\}$  can exist in four definite symmetry combinations: symmetric (S), mixed-symmetric (MS), mixed antisymmetric (MA) and totally antisymmetric (A)<sup>2</sup>; projection operators that generate these combinations are specified in the Appendix, in Eqs. (A1) and (A2). We will write our baryon interpolating operators by applying projection operators that act on the flavor, spin and spatial labels of a generic three-quark operator,  $\psi_1\psi_2\psi_3$ :

$$B = (\mathcal{F}_{\Sigma_F} \otimes \mathcal{S}_{\Sigma_S} \otimes \mathcal{D}_{\Sigma_D}) \{\psi_1\psi_2\psi_3\},$$

where  $\mathcal{F}, \mathcal{S}$  and  $\mathcal{D}$  are flavor, Dirac spin and spatial projection operators, respectively, and the subscripts  $\Sigma_F, \Sigma_S$  and  $\Sigma_D$  specify the symmetry combinations of flavor, Dirac spin and spatial labels. For each operator  $B$ , we must combine the symmetry projection operators such that the resulting baryon operator is overall symmetric. The rules for combining symmetries of such direct products are given in Eq. (A3).

To illustrate the construction, we specialize to the case of local or quasi-local operators, where the spatial dependence is the same for each quark, and thereby symmetric. Thus we write this simplified interpolating operator as

$$B = (\mathcal{F}_{\Sigma_F} \otimes \mathcal{S}_{\Sigma_S}) \{\psi_1\psi_2\psi_3\}.$$

Furthermore, we will only consider the case of two-component Pauli spin rather than four-component Dirac spin. In the standard convention, Pauli spin involves a label  $s$  that can take two values:  $+$  and  $-$ . It is straightforward to extend the construction to Dirac spins using the Dirac-Pauli representation of Dirac matrices, as in Refs. [6, 7]. Dirac spins involve direct products of two Pauli spin representations: one for  $s$ -spin and the other for  $\rho$ -spin (intrinsic parity). The operator construction for Dirac spin is described in Appendix A.

The product rules of Eq. (A3) specify three ways to combine these flavor and spin projectors to yield an over-

all symmetric projector:

$$\mathcal{F}_S \mathcal{S}_S \quad (5)$$

$$\mathcal{F}_A \mathcal{S}_A \quad (6)$$

$$\frac{1}{\sqrt{2}} (\mathcal{F}_{MS} \mathcal{S}_{MS} + \mathcal{F}_{MA} \mathcal{S}_{MA}) \quad (7)$$

The four symmetric spin combinations  $\mathcal{S}_S$  simply correspond to the four states or operators of spin  $\frac{3}{2}$ :  $\{++++\}_S, \{+++-\}_S, \{+- -\}_S, \{----\}_S$ , while the two mixed symmetric and two mixed antisymmetric combinations each correspond to states or operators of spin  $\frac{1}{2}$ ; there is no antisymmetric combination of three objects taking only two values.

For the case of  $SU(3)$  flavor, the flavor-symmetric combination  $\mathcal{F}_S$  yields the decuplet (10). Hence Eq. (5), with  $\mathcal{F}_S \rightarrow \{uuu\}$ , specifies the operators for the spin- $\frac{3}{2}$   $\Delta^{++}$ . The mixed-symmetric combinations  $\mathcal{F}_{MS,MA}$  specify the octet (8), so that  $\{udu\}_{MA,MS}$  correspond to the Nucleon. Thus we see that Eq. (7) specifies the operators for the spin- $\frac{1}{2}$  octet. Since there is no  $\mathcal{S}_A$  spin combination, this example cannot provide flavor-singlet (1) interpolating operators - angular structure through non-local behavior is required.

Covariant derivatives defined as in Ref. [6] are incorporated into the three-quark operators in order to obtain suitable representations that transform like orbital angular momentum. This is necessary in order to obtain operators with total angular momentum  $J > \frac{3}{2}$ . First the covariant derivatives are combined in definite symmetries with respect to their action on the three quark fields. A single derivative is constructed from  $\{\vec{D} \mathbb{1} \mathbb{1}\}_{\Sigma_D}$ . There are two relevant symmetry combinations,

$$L = 1 : \begin{cases} D_{MS}^{[1]} = \frac{1}{\sqrt{6}} (2D^{(3)} - D^{(1)} - D^{(2)}) \\ D_{MA}^{[1]} = \frac{1}{\sqrt{2}} (D^{(1)} - D^{(2)}) \end{cases} \quad (8)$$

where the notation  $D^{(q)}$  means that the derivative acts on the  $q$ -th quark. There is no totally antisymmetric construction of one derivative and the symmetric combination  $D^{(1)} + D^{(2)} + D^{(3)}$  is a total derivative that gives zero when applied to a baryon with zero momentum - it is omitted. Each derivative additionally has a direction index (suppressed above) for which we choose a circular basis such that they transform under rotations like components of a spin-1 object:

$$\begin{aligned} D_{m=\pm 1} &= \pm \frac{i}{2} (D_x \pm iD_y) \\ D_{m=0} &= -\frac{i}{\sqrt{2}} D_z. \end{aligned}$$

Totally symmetric baryon operators with one derivative are constructed by applying Eq. (8) to the mixed symmetry spin-flavor operators according to the rules given in Eq. (A3),

$$\psi_S^{[1]} = \frac{1}{\sqrt{2}} (D_{MS}^{[1]} \psi_{MS}^{[0]} + D_{MA}^{[1]} \psi_{MA}^{[0]}),$$

where superscripts in brackets indicate the number of derivatives in the operator.

<sup>2</sup> Mixed symmetry combinations are of definite symmetry under exchange of the first two objects.

$J$	irreps, $\Lambda(\text{dim})$
$\frac{1}{2}$	$G_1(2)$
$\frac{3}{2}$	$H(4)$
$\frac{5}{2}$	$H(4) \oplus G_2(2)$
$\frac{7}{2}$	$G_1(2) \oplus H(4) \oplus G_2(2)$
$\frac{9}{2}$	$G_1(2) \oplus {}^1H(4) \oplus {}^2H(4)$

TABLE II: Continuum spins subduced into lattice irreps  $\Lambda(\text{dim})$ . There are two embeddings of  $H$  in  $J = \frac{9}{2}$ .

Two derivative operators can be formed in definite three-quark symmetry combinations that transform like  $L = 0, 1, 2$  as follows,

$$L = 0, 2 : D_S^{[2]} = \frac{1}{\sqrt{2}}(+D_{MS}^{[1]}D_{MS}^{[1]} + D_{MA}^{[1]}D_{MA}^{[1]}), \quad (9)$$

$$L = 0, 2 : D_{MS}^{[2]} = \frac{1}{\sqrt{2}}(-D_{MS}^{[1]}D_{MS}^{[1]} + D_{MA}^{[1]}D_{MA}^{[1]}), \quad (10)$$

$$L = 0, 2 : D_{MA}^{[2]} = \frac{1}{\sqrt{2}}(+D_{MS}^{[1]}D_{MA}^{[1]} + D_{MA}^{[1]}D_{MS}^{[1]}), \quad (11)$$

$$L = 1 : D_A^{[2]} = \frac{1}{\sqrt{2}}(+D_{MS}^{[1]}D_{MA}^{[1]} - D_{MA}^{[1]}D_{MS}^{[1]}). \quad (12)$$

The projection into  $L = 0, 1, 2$  comes from combining a pair of derivatives via their (suppressed) direction indices using an  $SO(3)$  Clebsch-Gordan coefficient, i.e. as  $\langle 1, m_1; 1, m_2 | L, M \rangle D_{m_1} D_{m_2}$ .

Although it is allowed, we omit the  $D_S^{[2]}$  combination that couples to  $L = 0$ . It corresponds to the spatial Laplacian and vanishes at zero momentum. Several possibilities occur when totally symmetric baryon operators are formed using the rules of Eq. (A3) to combine the spatial derivatives and spins,

$$\psi_S^{[2]} = D_S^{[2]}\psi_S^{[0]}, \quad \frac{1}{\sqrt{2}}(D_{MS}^{[2]}\psi_{MS}^{[0]} + D_{MA}^{[2]}\psi_{MA}^{[0]}), \quad D_A^{[2]}\psi_A^{[0]},$$

where no total derivatives are formed from these constructions. The angular momenta of spinors and derivatives are combined using the standard Clebsch-Gordan formula of  $SU(2)$  in order to obtain operators with good  $J$  in the continuum,

$$|[J, M]\rangle = \sum_{m_1, m_2} |[J_1, m_1]\rangle \otimes |[J_2, m_2]\rangle \langle J_1 m_1; J_2 m_2 | JM \rangle.$$

The scheme outlined in this section provides a classification of all baryon operators constructed from three quarks with either light or strange masses, up to two derivatives in their spatial structure and respecting classical continuum symmetries.

A naming convention for such operators is useful. A Nucleon operator, with spin and parity of the three quarks equal to  $\frac{3}{2}^-$ , two derivatives coupled into  $L = 2$  and total spin and parity  $J^P = \frac{7}{2}^-$ , is denoted as

$$\left(N_M \otimes \left(\frac{3}{2}^-\right)_M^I \otimes D_{L=2,S}^{[2]}\right)^{J=\frac{7}{2}}, \quad (13)$$

	$I$	$S$	$G_1$	$H$	$G_2$
$N$	$\frac{1}{2}$	0	28	48	20
$\Delta$	$\frac{3}{2}$	0	15	26	11
$\Lambda$	0	0	41	60	29
$\Sigma$	1	-1	43	74	31
$\Xi$	$\frac{1}{2}$	-2	43	74	31
$\Omega$	0	-3	15	26	11

	$G_1$	$H$	$G_2$
Singlet, <b>1</b>	13	22	9
Octet, <b>8</b>	28	48	20
Decuplet, <b>10</b>	15	26	11

TABLE III: (left) Number of distinct operators, categorized by  $SU(3)_F$  in each lattice irrep  $\Lambda_{g,u}$ , using operators with up to two derivatives. (right) Number of distinct operators, categorized by  $SU(2)_F$  isospin ( $I$ ) and strangeness ( $S$ ) in each lattice irrep  $\Lambda_{g,u}$ , using operators with up to two derivatives. Each operator has  $\dim(\Lambda)$  “rows”. There are equal numbers of operators in positive and negative parity.

where subscripts show that the flavor construction is mixed symmetry ( $M$ ), the spin construction also is mixed symmetry and the two derivatives are in a symmetric combination ( $S$ ) as in Eq. (9). Direct products of these flavor, spin and space constructions yield an overall symmetric set of flavor, spin and spatial labels, as required.

A spin state like  $\left(\frac{3}{2}^-\right)$  can be constructed in several ways because Dirac spinors are used and they have four components, two upper and two lower components. A superscript  $1$  attached to the spin part indicates that the operator is the first of several embeddings with the same quantum numbers. Because of this, the basis set presented here is over-complete since operators featuring both derivatives and lower components are specified. However, this redundancy is intentional as we need a basis with multiple operators in each irrep for use with the variational method. If only Pauli spinors were used, we would have an  $SU(6) \otimes O(3)$  classification of operators. That subset of our operators is referred to as “non-relativistic”.

We reiterate that the operator construction described here provides a basis set for spectrum calculations. We are not forcing the symmetries manifested in the operator basis into the spectrum results to be shown later. Rather, the dynamics of QCD will decide on the eigenstates, which can correspond to any linear superpositions of the operator basis which may exhibit quite different symmetries to those diagonalised by this basis.

## B. Subduction

In lattice QCD calculations the theory is discretized on a four-dimensional Euclidean grid. The full three-dimensional rotational symmetry that classifies energy eigenstates in the continuum is reduced to the symmetry group of a cube (the cubic symmetry group, or equivalently the octahedral group). Instead of the infinite number of irreducible representations labelled by spin and parity,  $J^P$ , the double-cover cubic group for half-integer spin has only six irreducible representations (*ir*-

reps):  $G_{1g}, H_g, G_{2g}, G_{1u}, H_u, G_{2u}$ , where parity is denoted by the  $g$  (gerade) subscript for positive parity or the  $u$  (ungerade) subscript for negative parity. The distribution of the various  $M$  components of a spin- $J$  baryon into the lattice irreps is known as *subduction*, the result of which is shown in Table II.

Extending the analysis of Refs. [16, 17] to baryons, we use “subduction” matrices for half-integer spins to project the continuum-based operators to irreducible representations of the octahedral group,

$$\mathcal{O}_{n\Lambda,r}^{[J]} = \sum_M \mathcal{S}_{n\Lambda,r}^{J,M} \mathcal{O}^{[J,M]}, \quad (14)$$

where  $\mathcal{O}^{[J,M]}$  is a lattice operator constructed as outlined in Appendix (A3). As seen in Table II, subduction of  $J = \frac{9}{2}$  yields two occurrences of the  $H$  irrep. Multiple occurrences of lattice irreps are the general rule for spins higher than 4. We denote by  ${}^n\Lambda$  the  $n^{\text{th}}$  occurrence of irrep  $\Lambda$  in the subduction of spin  $J$ . For example, the two occurrences of octahedral irrep  $H$  in the subduction of  $J = \frac{9}{2}$  are denoted as  ${}^1H$  and  ${}^2H$ . For each  $J \rightarrow {}^n\Lambda$  there is a subduction matrix  $\mathcal{S}$  in the values of  $M$  and the rows of the irrep,  $r$ , that maps the continuum spin operators to irreducible representations of the octahedral group. These subduction matrices are derived for half-integer spins up to  $\frac{9}{2}$  in Appendix B and the resulting matrices are tabulated in Appendix B.

Classifying operators by  $SU(3)_F$  symmetry, we have the total number of operators in each lattice irrep as shown in Table III(left). Considered as a broken symmetry with an unbroken  $SU(2)_F$  isospin symmetry, we have the number of operators shown in Table III(right). The operator basis used in this work is constructed using  $SU(3)_F$  flavor symmetry. Of course, the  $SU(3)_F$  symmetry is broken in QCD, most notably by the mass of the strange quark. The  $SU(3)_F$  operator basis allows the flavor symmetry breaking to be determined by the relative degree of overlap onto operators transforming in different representations of  $SU(3)_F$ . This is comparable to what is done in quark models and other approaches, which helps to relate the lattice results to phenomenology.

With the construction of operators and their subduction to irreps of the cubic group outlined as above, we defer further details to the appendices. Appendix A provides details of the operator constructions, Appendix B derives the subduction matrices through an analysis of the quantum mechanics of continuum spin in the octahedral representation, and Appendix B provides the subduction matrices for half-integer spins.

## V. CORRELATOR ANALYSIS

The variational method for spectral extraction [12–14], which takes advantage of the multiplicity of operators within a given symmetry channel to find the best (in a variational sense) linear combination of operators for each state in the spectrum, is now in common

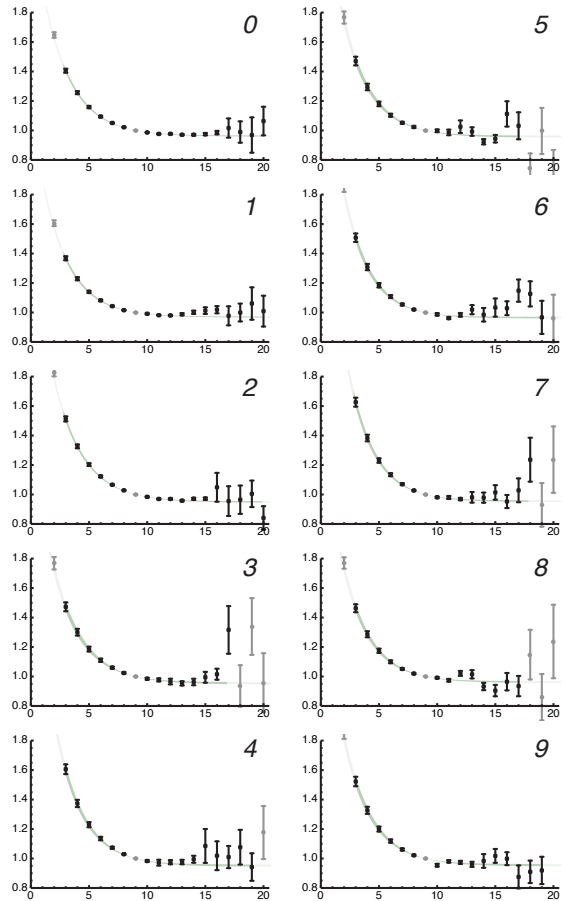


FIG. 1: Principal correlator fits according to Eq. (17). For ten states of the Nucleon  $H_u$  irrep for  $m_\pi = 524$  MeV, the plots show  $\lambda^n(t) \cdot e^{m_n(t-t_0)}$  data and the fit for  $t_0 = 9$ . Data used in the fit are shown in black, while points excluded from the fit are in grey.

usage[15, 20–23]. Our application of the method follows that developed in Refs. [16, 17, 24], and applied to the analysis of the excited meson spectrum, and we summarize it here.

The starting point is the system of generalized eigenvalue equations for the correlation matrix:

$$C(t)v^n(t) = \lambda_n(t)C(t_0)v^n(t) \quad (15)$$

where  $\lambda_n(t_0) = 1$ , and where there is an orthogonality condition on the eigenvectors of different states ( $\mathbf{n}, \mathbf{n}'$ ),  $v^{\mathbf{n}'\dagger}C(t_0)v^\mathbf{n} = \delta_{\mathbf{n},\mathbf{n}'}$ . This orthogonality condition provides eigenvectors that distinguish clearly between nearly degenerate states, which would be difficult to distinguish by their time dependence alone. Equation (15) is solved for eigenvalues,  $\lambda_n$ , and eigenvectors,  $v^\mathbf{n}$ , independently on each timeslice,  $t$ . Rather than ordering the states by the size of their eigenvalue, which can become uncertain because of the high level of degeneracy in the baryon

spectrum, we associate states at different timeslices using the similarity of their eigenvectors. We choose a reference timeslice on which reference eigenvectors are defined,  $v_{\text{ref}}^{\mathbf{n}} \equiv v^{\mathbf{n}}(t_{\text{ref}})$ , and compare eigenvectors on other timeslices by finding the maximum value of  $v_{\text{ref}}^{\mathbf{n}'} C(t_0) v^{\mathbf{n}}$  which associates a state  $\mathbf{n}$  with a reference state  $\mathbf{n}'$ . Using this procedure we observe essentially no “flipping” between states in either the principal correlators,  $\lambda_{\mathbf{n}}(t)$ , or the eigenvectors,  $v^{\mathbf{n}}(t)$ , as functions of  $t$ .

Any two-point correlation function on a finite spatial lattice can be expressed as a spectral decomposition

$$C_{ij}(t) = \sum_{\mathbf{n}} \frac{Z_i^{\mathbf{n}*} Z_j^{\mathbf{n}}}{2m_{\mathbf{n}}} e^{-m_{\mathbf{n}} t} \quad (16)$$

where we assume that  $t \ll L_t$ , the temporal length of the box, so that the opposite-parity contributions arising from the other time ordering on the periodic lattice can be ignored. The “overlap factors”,  $Z_i^{\mathbf{n}} \equiv \langle \mathbf{n} | \mathcal{O}_i^\dagger | 0 \rangle$  are related to the eigenvectors by  $Z_i^{\mathbf{n}} = \sqrt{2m_{\mathbf{n}}} e^{m_{\mathbf{n}} t_0/2} v_j^{\mathbf{n}*} C_{ji}(t_0)$ .

We obtain the masses from fitting the principal correlators,  $\lambda_{\mathbf{n}}(t)$ , which for large times should tend to  $e^{-m_{\mathbf{n}}(t-t_0)}$ . In practice we allow a second exponential in the fit form, and our fit function is

$$\lambda_{\mathbf{n}}(t) = (1 - A_{\mathbf{n}}) e^{-m_{\mathbf{n}}(t-t_0)} + A_{\mathbf{n}} e^{-m'_{\mathbf{n}}(t-t_0)}, \quad (17)$$

where the fit parameters are  $m_{\mathbf{n}}, m'_{\mathbf{n}}$  and  $A_{\mathbf{n}}$ . Typical fits for a set of excited states within an irrep are shown in Figure 1 where we plot the principal correlator with the dominant time-dependence due to state  $\mathbf{n}$  divided out. If a single exponential were to dominate the fit, such a plot would show a constant value of unity for all times. For the form of Eq. 17, the data would approach a constant  $1 - A$  at large times, and this is clearly satisfied for  $t > t_0$ .

Empirically we find that the size of the second exponential term decreases rapidly as one increases  $t_0$ . Further we find, in agreement with the perturbative analysis of Ref. [14] and with our earlier meson analysis, that for large  $t_0$  values the  $m'_{\mathbf{n}}$  extracted are larger than the value of  $m_{\mathbf{n}=\text{dim}(C)}$ , the largest “first” exponential mass extracted. At smaller  $t_0$  values this is not necessarily true and is indicative of an insufficient number of states in Eq. (16) to describe  $C(t_0)$  completely. The values of  $A_{\mathbf{n}}$  and  $m'_{\mathbf{n}}$  are not used elsewhere in the analysis.

Our choice of  $t_0$  is made using the “reconstruction” scheme[17, 24]: the masses,  $m_{\mathbf{n}}$ , extracted from the fits to the principal correlators, and the  $Z_i^{\mathbf{n}}$  extracted from the eigenvectors at a single time slice are used to reconstruct the correlator matrix using Eq. (16). This reconstructed matrix is then compared with the data for  $t > t_0$ , with the degree of agreement indicating the acceptability of the spectral reconstruction. Adopting too small a value of  $t_0$  leads to a poor reconstruction of the data for  $t > t_0$ . In general, the reproduction is better as  $t_0$  is increased until increased statistical noise prevents further improvement. The sensitivity of extracted spectral quantities to

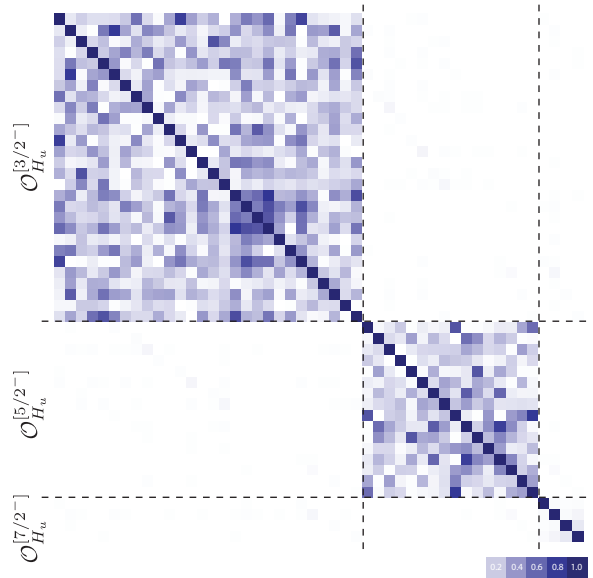


FIG. 2: The magnitude of matrix elements in a matrix of correlation functions,  $C_{ij}/\sqrt{C_{ii}C_{jj}}$ , at time-slice 5 is shown according to the scale at the lower right. The matrix is for the Nucleon  $H_u$  irrep, with 28 [ $J = \frac{3}{2}$ ] operators, 16 [ $J = \frac{5}{2}$ ] operators and 4 [ $J = \frac{7}{2}$ ] operators.

the value of  $t_0$  used will be discussed in detail in section VII A, but in short the energies of low-lying states are rather insensitive to  $t_0$  and the reconstruction of the full correlator matrix usually is best when  $t_0 \gtrsim 7$ , but not too large.

From the spectral decomposition of the correlator, equation 16, it is clear that there should in fact be no time dependence in the eigenvectors. Because of states at higher energies than can be resolved with  $\text{dim}(C)$  operators, there generally is a contribution to energies and  $Z$ 's that decays more rapidly than the lowest mass state that contributes to a principal correlator. As for energies, we obtain “time-independent” overlap factors,  $Z_i^{\mathbf{n}}$  from fits of  $Z_i^{\mathbf{n}}(t)$ , obtained from the eigenvectors, with a constant or a constant plus an exponential, in the spirit of the perturbative corrections outlined in [14]).

## VI. DETERMINING THE SPIN OF A STATE

### A. Motivation and procedure

A new method for identifying the spins of excited mesonic states was introduced in Refs. [16, 17]. In this work, we extend the method to identify spins of excited baryonic states. The explanation for the success of the new method is that there is an approximate realization of rotational invariance at the scale of hadrons in our correlation functions. There are two reasons for this claim.

The first is that there are no dimension-five operators made of quark bilinears that respect the symmetries of lattice actions based on the Wilson formalism and that do not also transform trivially under the continuum group of spatial rotations. Thus, rotational symmetry breaking terms do not appear until  $\mathcal{O}(a^2)$  in the action. This argument holds even though the action used in this work describes an anisotropic lattice. The second reason is that our baryon operators are constructed from low momentum filtered, smeared quark fields, where the smearing is designed to filter out fluctuations on small scales. Possible divergent mixing with lower dimensional operators is then expected to be suppressed. The baryon operators then are reasonably smooth on a size scale typical of baryons, which is  $R \approx 1$  fm. With the lattice spacing of  $\sim 0.12$  fm, the breaking of rotational symmetry in the action or the baryon operators can be small:  $(a/R)^2 \approx 0.015$ . Of course, these qualitative arguments should be backed up by evidence of approximate rotational invariance in explicit calculation.

The operators constructed in Section IV using subduction matrices transform irreducibly under the allowed cubic rotations, that is they faithfully respect the symmetries of the lattice. They also carry information about the continuum angular momentum,  $J$ , from which they are subduced. To the extent that approximate rotational invariance is realized, we expect that an operator subduced from spin  $J$  to overlap strongly only onto states of continuum spin  $J$ , and have little overlap with states of different continuum spin. In fact this is clearly apparent even at the level of the correlator matrix as seen in Figure 2. Here the correlator matrix for the Nucleon  $H_u$  is observed to be approximately block diagonal when the operators are ordered according to the spin from which they were subduced.

To identify the spin of a state, we use the operator “overlaps”  $Z_i^n = \langle n | \mathcal{O}_i^\dagger | 0 \rangle$  for a given state extracted through the variational method presented in the previous section. In Figure 3 we show the overlaps for a set of low-lying states in the Nucleon  $H_u$  and  $G_{2u}$  irreps of the  $m_\pi = 524$  MeV  $16^3$  calculation. The principal correlators for these states in  $H_u$  are shown in Figure 1, and the corresponding mass spectrum is shown in Figure 9. The overlaps for a given state show a clear preference for overlap onto only operators of a single spin. While we show only a subset of the operators for clarity, the same pattern is observed for the full operator set.

The assignment of spin must hold for states with continuum spin  $J$  subduced across multiple irreps. In the continuum our operators are of definite spin such that  $\langle 0 | \mathcal{O}^{J,M^\dagger} | J', M' \rangle = Z^{[J]} \delta_{J,J'} \delta_{M,M'}$ , and therefore from Eq. 14 the overlap of the subduced operator is  $\langle 0 | \mathcal{O}_{n\Lambda,r}^{[J]\dagger} | J', M \rangle = \mathcal{S}_{n\Lambda,r}^{J,M} Z^{[J]} \delta_{J,J'}$ . Only the spin  $J$  states will contribute, and not any of the other spins present in the irrep  $n\Lambda$ . Inserting a complete set of hadronic states between the operators in the correlator and using the fact that the subduction coefficients form an orthogonal matrix (B7),  $\sum_M \mathcal{S}_{\Lambda,\Lambda'}^{J,M} \mathcal{S}_{\Lambda',r'}^{J,M} = \delta_{\Lambda,\Lambda'} \delta_{r,r'}$ , we thus obtain

terms in the correlator spectral decomposition proportional to  $Z^{[J]*} Z^{[J]}$  for each  $\Lambda$  we have subduced into, up to discretization uncertainties as described above. Hence, for example, a  $J = \frac{7}{2}$  baryon created by a  $[J = \frac{7}{2}]$  operator will have the same  $Z$  value in each of the  $G_1, H, G_2$  irreps. This suggests that we compare the independently obtained  $Z$ -values in each irrep. In Figure 4 we show the extracted  $Z$  values for negative-parity states suspected of being spin  $\frac{5}{2}$  across the  $H_u$  and  $G_{2u}$  irreps, and of being spin  $\frac{7}{2}$  across the  $G_{1u}, H_u$  and  $G_{2u}$  irreps. As can be seen, there is good agreement of  $Z$  values in the different irreps that are subduced from spin  $J$ , with only small deviations from exact equality.

These results demonstrate that the  $Z$  values of carefully constructed subduced operators can be used to identify the continuum spin of states extracted in explicit computation for the lattices and operators we have used.

We take the next step and use the identification of the components of the spin- $J$  baryon subduced across multiple irreps to make a best estimate of the mass of the state. The mass values determined from fits to principal correlators in each irrep differ slightly due to what we assumed to be discretization effects and, in principle, avoidable fitting variations (such as the fitting intervals). We follow Ref. [17] and perform a joint fit to the principal correlators with the mass being common. This method provides a numerical test that the state has been identified. We allow a differing second exponential in each principal correlator so that the fit parameters are  $m_n, \{m_n'^\Lambda\}$  and  $\{A_n^\Lambda\}$ . These fits are typically very successful with correlated  $\chi^2/N_{\text{dof}}$  close to 1, suggesting again that the discretization effects are small. An example for the case of  $\frac{7}{2}^-$  components identified in  $G_{1u}, H_u, G_{2u}$  is shown in Figure 5. When we present our final, spin-assigned spectra it is the results of such fits that we show.

## B. Additional demonstration of approximate rotational invariance

A further demonstration of approximate rotational invariance is based on the spectrum of energy levels. If indeed the mixing between states of different continuum spin  $J$  is small, then the omission of such coupling should not much affect the excited state spectra. That proposition can be tested by extracting energies using all operators, and comparing them with the energies obtained from only operators subduced from a single  $J$  value. If approximate rotational invariance were achieved in the spectrum, the energies would be nearly the same. As an example, we show results for the Nucleon  $H_u$  irrep, in Fig. 6. The left column of the Fig. 6, labelled “all”, shows the lowest 12 energy levels obtained from matrices of correlation functions using the set of all 48  $H_u$  operators, and spin identified using the methods previously described. The states listed in Figure 3 correspond to a few of these 12 levels. The second column shows the lowest 6 levels resulting from the variational method when



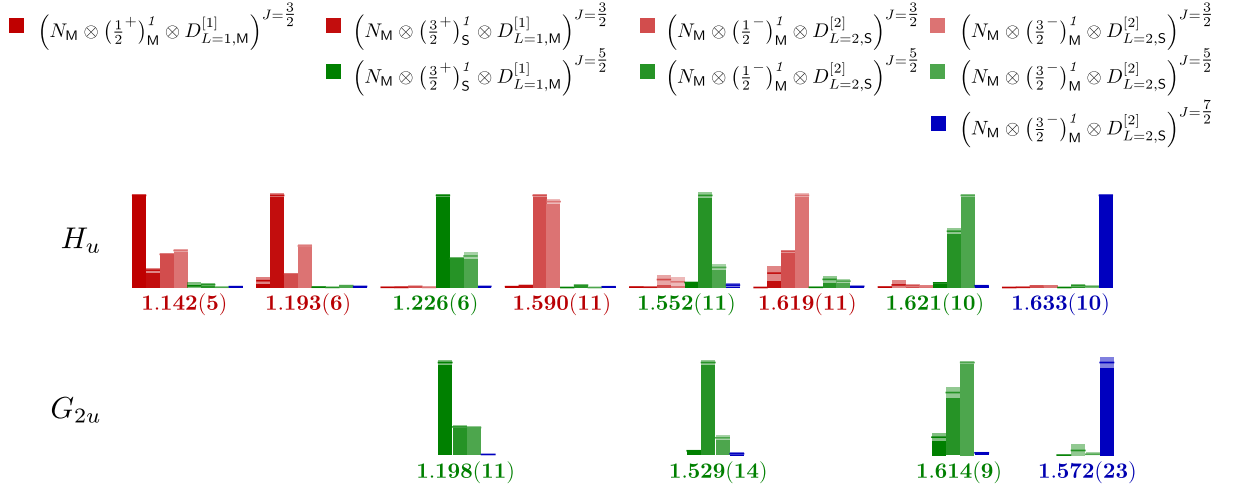


FIG. 3: Histograms of spectral overlaps,  $Z$ , are shown for a selection of eight operators (shown at the top using the naming convention of Eq. (13)). The 4 operators labelled with  $J = \frac{3}{2}$  (color red) have subductions only to the  $H_u$  irrep. The 3 operators labelled with  $J = \frac{5}{2}$  (color green) and the 1 labelled with  $J = \frac{7}{2}$  (color blue) have subductions to both  $H_u$  and  $G_{2u}$  irreps. Each histogram is labelled by the value of mass  $m$  of the state (in units of  $m_\Omega$ ) and has 8 vertical bars showing the relative  $Z$  values for each of the operators. The data are from the  $m_\pi = 524$  MeV ensemble and  $Z$ 's are normalized so that the largest value across all states, for a given operator, is equal to 1. The lighter area at the head of each bar represents the one sigma statistical uncertainty. Note that for each state only one or two operators have a large relative  $Z$  value, and it is the same operators appearing across each of the irreps. Note also that nearly the same energies are obtained in  $H_u$  and  $G_{2u}$  irreps for state subduced from one  $J$  value.

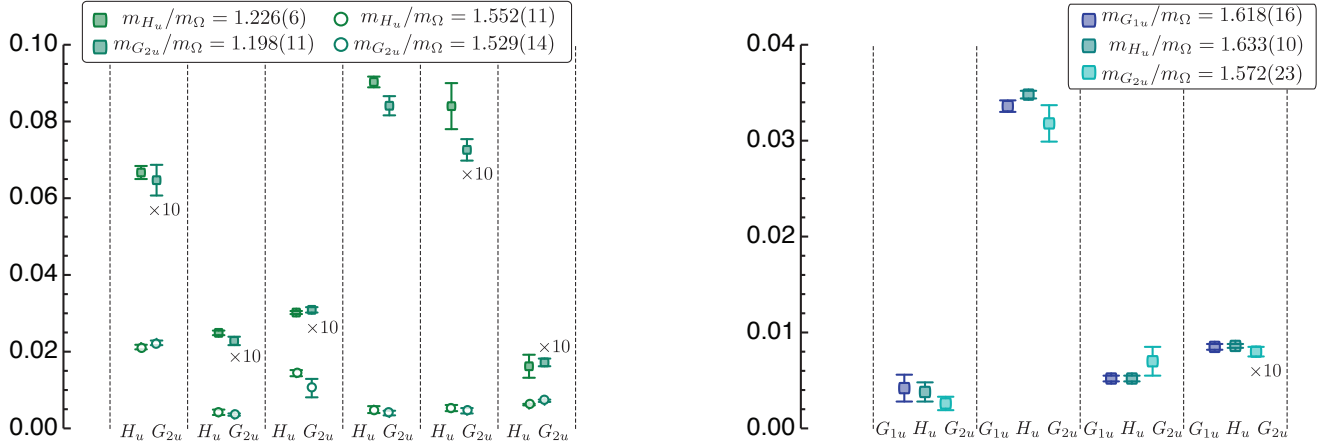


FIG. 4: Selected  $Z$  values across irreps  $\Lambda_u$  are shown for states suspected of being  $J = \frac{5}{2}$  (left panel) and  $J = \frac{7}{2}$  (right panel), based on the  $m_\pi = 524$  MeV ensemble. The boxes at the top show the mass for the various states. There are two states of  $J = \frac{5}{2}^-$ . The operators in the left panel, all projected onto  $J = \frac{5}{2}^-$ , are left to right,  $N_M \otimes (\frac{1}{2}^-)_M^I \otimes D_{L=2,S}^{[2]}$ ,  $N_M \otimes (\frac{1}{2}^-)_S^I \otimes D_{L=2,M}^{[2]}$ ,  $N_M \otimes (\frac{3}{2}^+)_M^I \otimes D_{L=1,M}^{[1]}$ ,  $N_M \otimes (\frac{3}{2}^+)_S^I \otimes D_{L=1,M}^{[1]}$ ,  $N_M \otimes (\frac{3}{2}^-)_M^I \otimes D_{L=2,S}^{[2]}$ ,  $N_M \otimes (\frac{3}{2}^-)_S^I \otimes D_{L=2,M}^{[2]}$ . Overlaps of these operators after subduction into  $H_u$  and  $G_{2u}$ , agree well for each of the two states shown. The operators in the right panel, all projected onto  $J = \frac{7}{2}^-$ , are left to right,  $N_M \otimes (\frac{3}{2}^-)_M^I \otimes D_{L=2,M}^{[2]}$ ,  $N_M \otimes (\frac{3}{2}^-)_M^I \otimes D_{L=2,S}^{[2]}$ ,  $N_M \otimes (\frac{3}{2}^-)_S^I \otimes D_{L=2,M}^{[2]}$ ,  $N_M \otimes (\frac{3}{2}^-)_S^I \otimes D_{L=2,S}^{[2]}$ . Similarly, the operator overlaps for this state agree well across  $G_{1u}$ ,  $H_u$ , and  $G_{2u}$ .

the operator basis is restricted to only those with continuum spin  $J = \frac{3}{2}$ . Similarly, the third shows the lowest 4 levels when the operator basis is restricted to only those with continuum spin  $J = \frac{5}{2}$ , and the last column are the lowest two levels when the basis is restricted to only  $J = \frac{7}{2}$  operators.

The results are striking. We see that the masses of the levels in each of the restricted bases agree quite well with the results found in the full basis. The agreement is quite remarkable because one expects operators in the  $H_u$  irrep that can couple with the ground state (the lowest  $J = \frac{3}{2}$  state), will allow for the rapid decay of correlators down

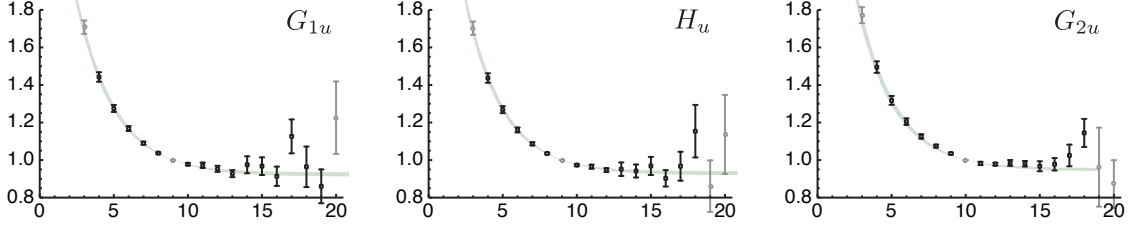


FIG. 5: Fit to the three subdued principal correlators of lowest lying  $\frac{7}{2}^-$  Nucleon using a common mass. Results are from the  $m_\pi = 524$  MeV ensemble. These levels correspond to the sixth excited  $G_{1u}$ , the seventh  $H_u$  and the fourth  $G_{2u}$ . Plotted is  $\lambda(t) \cdot e^{m(t-t_0)}$ . Grey points not included in the fit.

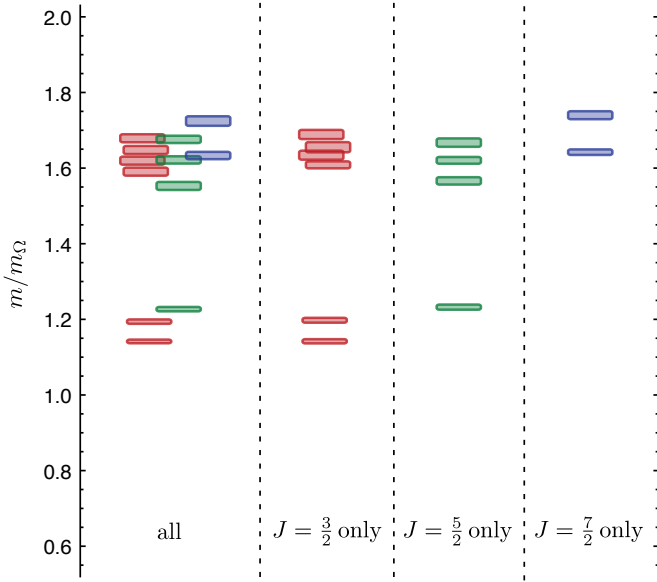


FIG. 6: Extracted Nucleon  $H_u$  mass spectrum for various operator bases. (a) Full basis (dim = 48), (b) Only  $J = \frac{3}{2}$  operators (dim = 28), (c) Only  $J = \frac{5}{2}$  operators (dim = 16), (d) Only  $J = \frac{7}{2}$  operators (dim = 4). Results are from the  $m_\pi = 524$  MeV ensemble. The dimensionality of the operator basis in each  $J$  is shown in Table A 3.

to the ground state as a function of time,  $t$ . However, the higher-energy spin  $\frac{5}{2}$  and  $\frac{7}{2}$  states do not show such a decay; we obtain good plateaus in plots like those in Fig. 1. These results provide rather striking demonstration for the lack of significant rotational symmetry breaking in the spectrum.

## VII. STABILITY OF SPECTRUM EXTRACTION

In this section we consider to what extent the extracted spectrum changes as we vary details of the calculation, such as the metric timeslice,  $t_0$ , used in the variational

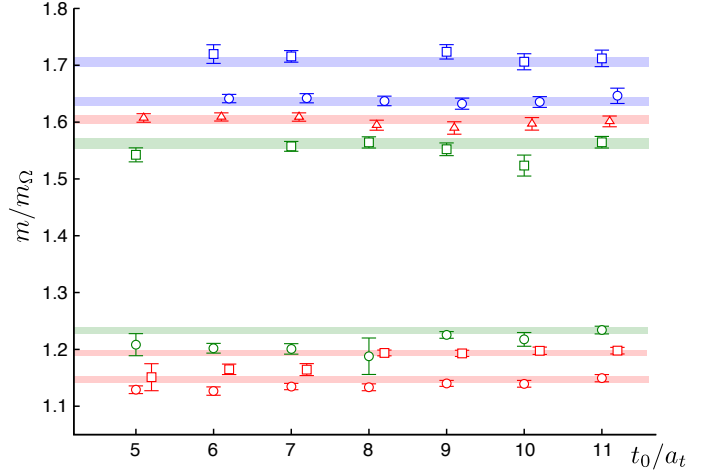


FIG. 7: Extracted Nucleon  $H_u$  mass spectrum as a function of  $t_0$ . Horizontal bands to guide the eye. For clarity of presentation, only one of the highly excited  $J = \frac{3}{2}^-$  and  $J = \frac{5}{2}^-$  levels are shown.

analysis, and the number of distillation vectors. We will use the Nucleon  $H_u$  and the Delta  $H_g$  irreps in the  $m_\pi = 524$  MeV dataset to demonstrate our findings.

### A. Variational analysis and $t_0$

Our fitting methodology was described in Section V where reconstruction of the correlator was used to guide us to an appropriate value of  $t_0$ . As seen in Figure 7, for  $t_0 \gtrsim 7$ , the low-lying mass spectrum is quite stable with respect to variations of  $t_0$ . This appears to be mostly due to the inclusion of a second exponential term in Eq. (17), which is able to absorb much of the effect of states outside the diagonalization space. The contribution of this second exponential typically falls rapidly with increasing  $t_0$  both by having a smaller  $A$  and a larger  $m'$ .

Overlaps,  $Z_n^i = \langle \mathbf{n} | \mathcal{O}_i^\dagger | 0 \rangle$ , can show more of a sensitivity to  $t_0$  values being too low, as was found also in the analysis of mesons, Ref. [17].

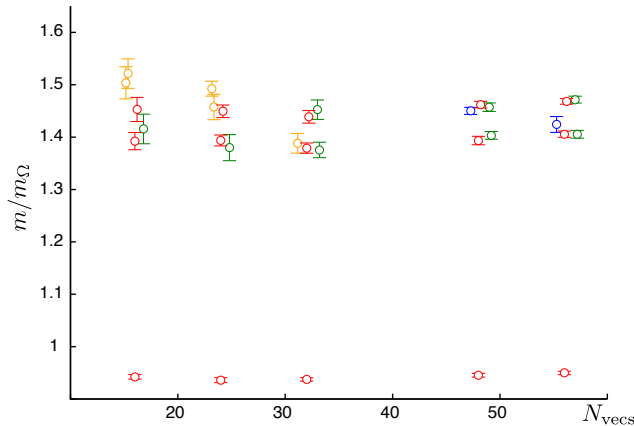


FIG. 8: Extracted the Delta  $H_g$  mass spectrum as a function of number of distillation vectors in the  $m_\pi = 524$  MeV dataset. For  $N \lesssim 32$ , spin identification is lost for the highest  $J = \frac{5}{2}^+$  and  $J = \frac{7}{2}^+$  levels.

In summary it appears that variational fitting is reliable provided  $t_0$  is “large enough”. Using two-exponential fits in principal correlators we observe relatively small  $t_0$  dependence of masses, but more significant dependence for the  $Z$  values which we require for spin-identification.

### B. Number of distillation vectors

The results presented so far are based on the analysis of correlators computed on  $16^3$  lattices using 56 distillation vectors. We consider how the determination of the spectrum varies if one reduces the number of distillation vectors and thus reduces the computational cost of the calculation. This is particularly important given that, as shown in [19], to get the same smearing operator on larger volumes one must scale up the number of distillation vectors by a factor equal to the ratio of spatial volumes. To scale up to a  $32^3$  lattice this would require  $56 \times (\frac{32}{16})^3 = 448$  vectors which is not currently a realizable number without using stochastic estimation [25].

In figure 8 we show the low-lying part of the extracted Delta  $H_g$  spectrum on the  $m_\pi = 524$  MeV lattice as a function of the number of distillation vectors used in the correlator construction. It is clear that the spectrum is reasonably stable for  $N \gtrsim 32$  but that the spectrum quality degrades rapidly for fewer vectors. In particular, the methods for spin identification fail for the highest  $J^P = \frac{5}{2}^+$  state as well as the first  $J^P = \frac{7}{2}^+$  state.

The need for a large numbers of distillation vectors has been discussed in Ref. [17] for the case of isovector mesons. The conclusion drawn is that to describe high spin hadrons having large orbital angular momentum, one needs to include sufficient vectors to sample the rapid

angular dependence of the wavefunction over the typical size of a hadron. The results for baryons presented here are consistent with these observations.

In summary one is limited as to how few distillation vectors can be used if one requires reliable extraction of high-spin states. The results shown here suggest 32 distillation vectors on a  $16^3$  lattice is the minimum, so at least 64 distillation vectors on a  $20^3$  lattice are likely to be required.

## VIII. RESULTS

Our results are obtained on  $16^3 \times 128$  lattices with pion masses between 396 and 524 MeV. More complete details of the number of configurations, time sources and distillation vectors used are given in Table I. The full basis of operators in each irrep listed in Table III is used for the variational method construction.

### A. $m_\pi = 524$ MeV results

Using the variational method outlined in Section V, the spectrum of energies in each lattice irrep for the Nucleon and for the Delta are shown in Figures 9 and 10, respectively. By applying the spin-identification procedure described above, we can subsequently associate continuum  $J^P$  labels to each of these states, as labelled on the figures. For the remainder of this paper, we will therefore label the energies by their assigned continuum spins; these are shown for the lattices at  $m_\pi = 524$  MeV in Figure 11, with the energies obtained from a joint fit to the principal correlators as described in Section V.

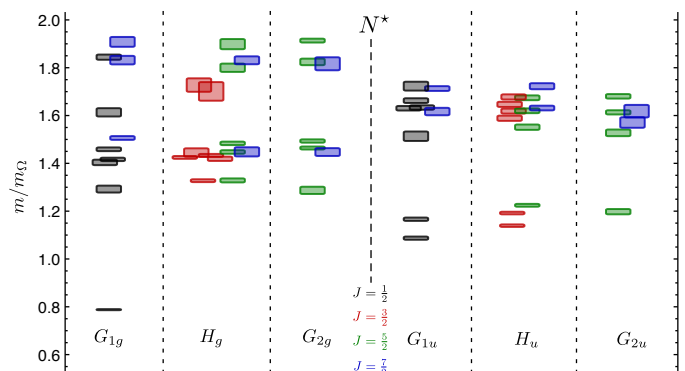


FIG. 9: Extracted Nucleon spectra by irrep for  $m_\pi = 524$  MeV. Colors are black ( $J = \frac{1}{2}$ ), red ( $\frac{3}{2}$ ), green ( $\frac{5}{2}$ ), blue ( $\frac{7}{2}$ ). Masses are shown in ratios of the  $\Omega$  baryon mass.

There are several notable features in these spectra. As we will discuss, the patterns of states have a good correspondence with single-hadron states as classified by  $SU(6) \otimes O(3)$  symmetry. The numbers of low-lying states in each  $J^P$  are similar to the numbers obtained in the

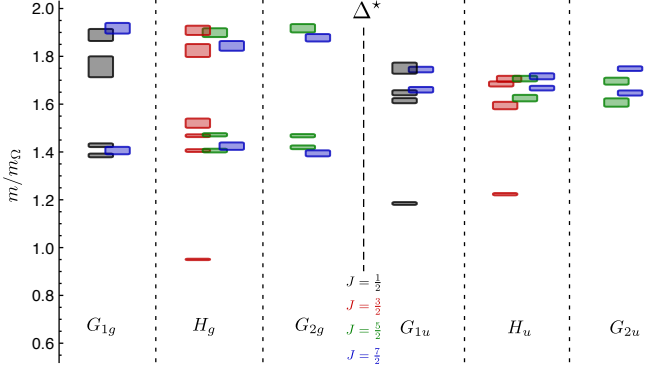


FIG. 10: Extracted Delta spectra by irrep for  $m_\pi = 524$  MeV. Colors are black ( $J = \frac{1}{2}$ ), red ( $\frac{3}{2}$ ), green ( $\frac{5}{2}$ ), blue ( $\frac{7}{2}$ ). Masses are shown in ratios of the  $\Omega$  baryon mass.

non-relativistic quark model which is a particular realisation of the symmetry above (e.g., [26, 27]). For the purposes of these comparisons, it is helpful to introduce a spectroscopic notation:  $X^{2S+1}L_\pi J^P$ , where  $X$  is the Nucleon  $N$  or the Delta  $\Delta$ ,  $S$  is the Dirac spin,  $L = S, P, D, \dots$  denotes the combined angular momentum of the derivatives,  $\pi = S, M, \text{ or } A$  is the permutational symmetry of the derivative, and  $J^P$  is the total angular momentum and parity. This notation also is used in Table IV, which we discuss now.

In the negative parity  $N^*$  spectrum, there is a pattern of five low-lying levels, consisting of two  $N^{\frac{1}{2}-}$  levels, two  $N^{\frac{3}{2}-}$  levels, and one  $N^{\frac{5}{2}-}$  level. The triplet of higher levels in this group of five is nearly degenerate with a pair of  $\Delta^{\frac{1}{2}-}$  and  $\Delta^{\frac{3}{2}-}$  levels. This pattern of Nucleon and Delta levels is consistent with an  $L = 1^-$   $P$ -wave spatial structure with mixed symmetry,  $P_M$ . As shown in Table IV, the same numbers of states are obtained in the  $SU(6) \otimes O(3)$  classification for the negative-parity Nucleon and Delta states constructed from the “non-relativistic” Pauli spinors as we find in the lattice spectra. The lowest two  $N^{*-}$  states are dominated by operators constructed in the notation of Eq. 13 as  $N_M \otimes (S = \frac{1}{2}^+)_{\text{M}} \otimes (L = 1^-)_{\text{M}} \rightarrow J^P = \frac{1}{2}^-$  and  $\frac{3}{2}^-$ , while the three higher  $N^{*-}$  levels are dominated by operators constructed according to  $N_M \otimes (S = \frac{3}{2}^+)_{\text{S}} \otimes (L = 1^-)_{\text{M}}$  with  $J^P = \frac{1}{2}^-$ ,  $\frac{3}{2}^-$  and  $\frac{5}{2}^-$ . Similarly, the low-lying Delta levels are consistent with a  $\Delta^{\frac{1}{2}-}$  and  $\Delta^{\frac{3}{2}-}$  assignment. There are no low-lying negative-parity  $S = \frac{3}{2}$  Delta states since a totally symmetric state (up to antisymmetry in color) cannot be formed. Consequently, there is no low-lying  $\Delta^{\frac{5}{2}-}$ , which agrees with the lattice spectrum. In the non-relativistic quark model [26], a hyperfine contact term is introduced to split the doublet and quartet states up and down, respectively, compared to unperturbed levels and the tensor part of the interaction provides some additional splitting. The result is that the doublet Delta states are nearly degenerate with the quartet Nucleon states as is observed in the lattice spectra, Fig. 11. In

Nucleon (8)			$SU(6) \otimes O(3)$	$n$
$J^P = \frac{1}{2}^-$	$N^2 P_{\frac{1}{2}}^{\frac{1}{2}-}$	$N^4 P_{\frac{1}{2}}^{\frac{1}{2}-}$	$[70, 1^-]$ $[70, 1^-]$	2
$J^P = \frac{3}{2}^-$	$N^2 P_{\frac{3}{2}}^{\frac{3}{2}-}$	$N^4 P_{\frac{3}{2}}^{\frac{3}{2}-}$	$[70, 1^-]$ $[70, 1^-]$	2
$J^P = \frac{5}{2}^-$		$N^4 P_{\frac{5}{2}}^{\frac{5}{2}-}$	$[70, 1^-]$	1
$J^P = \frac{1}{2}^+$	$N^2 S_{\frac{1}{2}}^{\frac{1}{2}+}$	$N^4 D_{\frac{1}{2}}^{\frac{1}{2}+}$	$[56, 0^+]$ $[70, 2^+]$	4
	$N^2 S_{\frac{3}{2}}^{\frac{1}{2}+}$		$[70, 0^+]$	
	$N^2 P_{\frac{1}{2}}^{\frac{1}{2}+}$		$[20, 1^+]$	
$J^P = \frac{3}{2}^+$	$N^2 D_{\frac{3}{2}}^{\frac{3}{2}+}$	$N^4 S_{\frac{3}{2}}^{\frac{3}{2}+}$	$[56, 2^+]$ $[70, 0^+]$	5
	$N^2 D_{\frac{5}{2}}^{\frac{3}{2}+}$	$N^4 D_{\frac{3}{2}}^{\frac{3}{2}+}$	$[70, 2^+]$ $[70, 2^+]$	
	$N^2 P_{\frac{3}{2}}^{\frac{3}{2}+}$		$[20, 1^+]$	
$J^P = \frac{5}{2}^+$	$N^2 D_{\frac{5}{2}}^{\frac{5}{2}+}$	$N^4 D_{\frac{5}{2}}^{\frac{5}{2}+}$	$[56, 2^+]$ $[70, 2^+]$	3
	$N^2 D_{\frac{7}{2}}^{\frac{5}{2}+}$		$[70, 2^+]$	
$J^P = \frac{7}{2}^+$		$N^4 D_{\frac{7}{2}}^{\frac{7}{2}+}$	$[70, 2^+]$	1

Delta (10)			$SU(6) \otimes O(3)$	$n$
$J^P = \frac{1}{2}^-$	$\Delta^2 P_{\frac{1}{2}}^{\frac{1}{2}-}$		$[70, 1^-]$	1
$J^P = \frac{3}{2}^-$	$\Delta^2 P_{\frac{3}{2}}^{\frac{3}{2}-}$		$[70, 1^-]$	1
$J^P = \frac{5}{2}^-$				0
$J^P = \frac{1}{2}^+$	$\Delta^2 S_{\frac{1}{2}}^{\frac{1}{2}+}$	$\Delta^4 D_{\frac{1}{2}}^{\frac{1}{2}+}$	$[70, 0^+]$ $[56, 2^+]$	2
$J^P = \frac{3}{2}^+$	$\Delta^2 D_{\frac{3}{2}}^{\frac{3}{2}+}$	$\Delta^4 S_{\frac{3}{2}}^{\frac{3}{2}+}$	$[70, 2^+]$ $[56, 0^+]$	3
		$\Delta^4 D_{\frac{3}{2}}^{\frac{3}{2}+}$	$[56, 2^+]$	
$J^P = \frac{5}{2}^+$	$\Delta^2 D_{\frac{5}{2}}^{\frac{5}{2}+}$	$\Delta^4 D_{\frac{5}{2}}^{\frac{5}{2}+}$	$[70, 2^+]$ $[56, 2^+]$	2
$J^P = \frac{7}{2}^+$		$\Delta^4 D_{\frac{7}{2}}^{\frac{7}{2}+}$	$[56, 2^+]$	1

TABLE IV: Subset of the operator basis classified by  $SU(6) \otimes O(3)$  multiplets and total spin and parity  $J^P$ . The entries are the orbital angular momentum structures outlined in Section IV and Appendix A that contribute within each  $J^P$ . The operators listed here are all from the first embedding in Dirac spin in Table VI, and correspond to only upper components (referred to as “non-relativistic”). A spectroscopic notation of  $X^{2S+1}L_\pi J^P$  is used, where  $X = N$  or  $\Delta$ ,  $S$  is the Dirac spin,  $L = S, P, D, \dots$  is the combined angular momentum of the derivatives,  $\pi = S, M, \text{ or } A$  is the permutational symmetry of the derivatives, and  $J^P$  is the total angular momentum and parity. In Sections IV-VI, an operator notation like  $(N_M \otimes (\frac{3}{2}^+)_{\text{S}} \otimes D_{L=1, \text{M}}^{[1]})^{J=\frac{5}{2}}$  was used which in this spectroscopic notation would be  $N^4 P_{\frac{5}{2}}^{\frac{5}{2}-}$ . Dimensions and parities of  $SU(6) \otimes O(3)$  representations are listed in column 4 for the doublet spin states of column 2, and in column 5 for the quartet spin states of column 3. The number,  $n$ , of operators for each  $J^P$  is listed in the rightmost column. This same spectroscopic notation and classification of spatial structure is also used for comparisons with models where  $L$  represents the orbital angular momentum.

the language of  $SU(6) \otimes O(3)$ , these low-lying  $N$  and  $\Delta$  states constitute the strangeness zero part of a  $[70, 1^-]$  multiplet, as indicated in Table IV.

In the positive parity sector, there also are interpretable patterns of lattice states in the range  $m/m_\Omega \sim 1.3 - 1.5$ . There are four  $N^{\frac{1}{2}+}$  levels, five  $N^{\frac{3}{2}+}$  levels, three  $N^{\frac{5}{2}+}$  levels and one  $N^{\frac{7}{2}+}$  level, which are the same numbers of levels for each  $J^P$  as in Table IV. The lattice

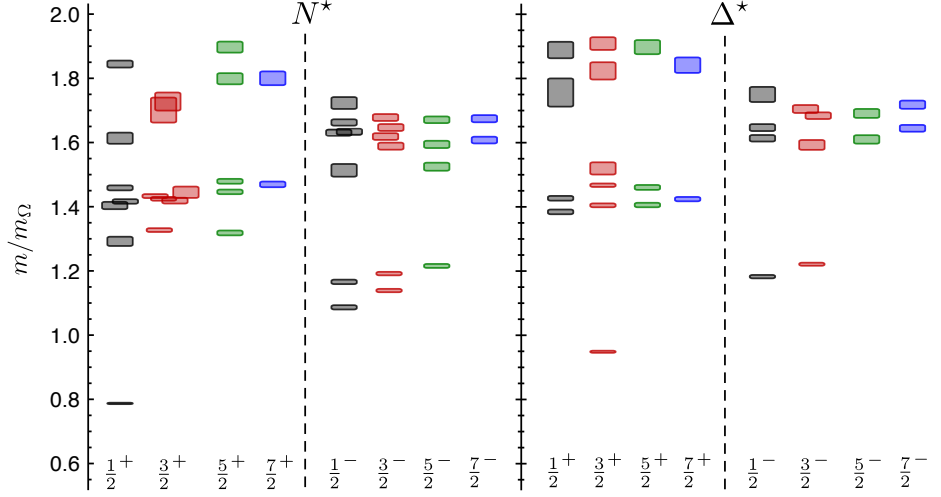


FIG. 11: Spin-identified spectrum of Nucleons and Deltas from the lattices at  $m_\pi = 524$  MeV, in units of the calculated  $\Omega$  mass.

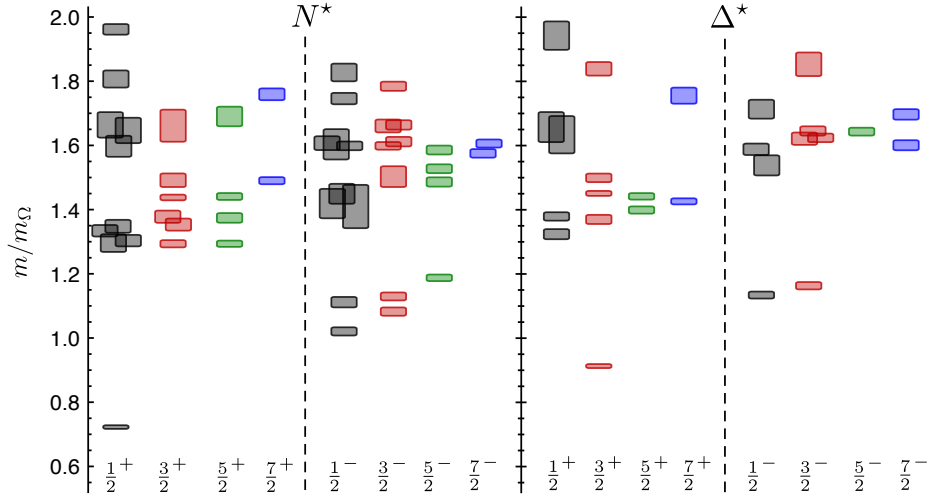


FIG. 12: Spin-identified spectrum of Nucleons and Deltas from the lattices at  $m_\pi = 396$  MeV, in units of the calculated  $\Omega$  mass.

spectra also have two  $\Delta_{\frac{1}{2}}^{1+}$  levels, three  $\Delta_{\frac{3}{2}}^{3+}$  levels, two  $\Delta_{\frac{5}{2}}^{5+}$  levels, and one  $\Delta_{\frac{7}{2}}^{7+}$  level, which are the same numbers of levels for each  $J^P$  as in Table IV. In this case we are considering the multiplets  $[70, 0^+]$ ,  $[56, 2^+]$ ,  $[70, 2^+]$ ,  $[20, 1^+]$  and a radially excited  $[56, 0^+]$  and within non-relativistic  $qqq$  constituent quark models [27], the mass eigenstates are admixtures of these basis states.

In general for both the Nucleon and Delta spectrum, there are reasonably well-separated bands of levels across the range of  $J$  values, alternating in parity, with each band higher in energy than the previous one. We remark that there are no obvious patterns of degenerate levels with opposite parities for the same total spin,  $J$  as in Ref. [28].

The discussion up to now has focused on observables; namely, the level energies. More information about the internal structure of the lattice states can be obtained by analyzing the spectral overlaps. We remind the reader that the full basis of operators listed in Table III is used within the variational method. We find that only a few operators have large overlaps in the lowest negative-parity Nucleon levels of the  $G_{1u}$ ,  $H_u$  and  $G_{2u}$  irreps, and these are the subdued versions of “non-relativistic” operators. From the construction of operators in Appendix A, those featuring only upper components in spin are in the first embedding of Dirac spin in Table VI. There is a one-to-one correspondence between these operators, and those listed in Table IV, and we will adopt the spectroscopic names as a shorthand. This spectro-

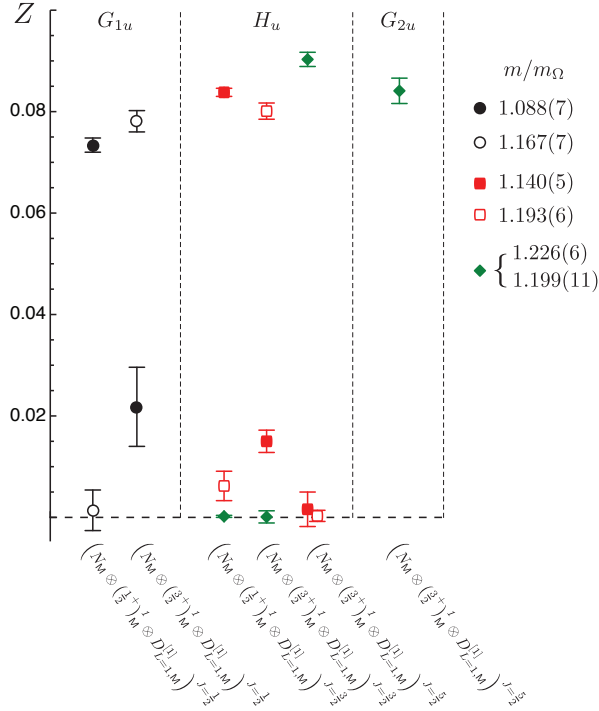


FIG. 13: Spectral overlaps for the negative parity Nucleon operators in Table IV within the lowest lying states for the  $m_\pi = 524$  MeV ensemble. The operators are subdivided into the  $G_{1u}$ ,  $H_u$  and  $G_{2u}$  irreps, and their spectral overlaps are shown for the lowest lying states with the masses listed in units of the  $\Omega$  baryon mass. In the spectroscopic notation, these are the  $N^2P_{M\frac{1}{2}}^-$  and  $N^4P_{M\frac{1}{2}}^-$  subdivided into  $G_{1u}$ , the  $N^2P_{M\frac{3}{2}}^-$  and  $N^4P_{M\frac{5}{2}}^-$  subdivided into  $H_u$ , and  $N^4P_{M\frac{5}{2}}^-$  subdivided into both  $H_u$  and  $G_{2u}$ . As can be seen, for each level one operator is dominant.

scopic notation is used in Table IV to identify operators, but is also applicable for identification of states. (Details of the derivative construction for the operators can be found in Appendix A 3.) The Nucleon (and Delta)  $J = \frac{1}{2}^-$ ,  $\frac{3}{2}^-$  and  $\frac{5}{2}^-$  operators all feature one derivative in  $P_M$  coupled to either a spin  $S = \frac{1}{2}$  (doublet) or  $S = \frac{3}{2}$  (quartet). Spectral overlaps ( $Z$ ) for these operators can be directly compared since they all have a consistent normalization. An  $S = \frac{3}{2}$  spin coupled to one derivative can be projected to either  $J = \frac{1}{2}$ ,  $J = \frac{3}{2}$  or  $J = \frac{5}{2}$ . The first and second constructions are subdivided into the  $G_{1u}$  and  $H_u$  irreps, while the  $J = \frac{5}{2}$  construction is subdivided into the  $H_u$  and  $G_{2u}$  irreps.

In Figure 13, we compare these non-relativistic operator overlaps for the lowest lying states and across irreps. We see that one operator is dominant for each state, with magnitudes that are roughly consistent across all irreps. In particular, the constructions coupled to different  $J$  have similar magnitudes. These results suggest that these

low-lying levels form a multiplet with little mixing among the states. In the language of  $SU(6) \otimes O(3)$  (spin-flavor and space), these states, and their negative parity Delta partners, are part of a  $[70, 1^-]$  multiplet.

Similarly, we can examine the first group of excited positive-parity levels in the Nucleon channel that cluster around  $m/m_\Omega \sim 1.4$ . Again, we find that the positive parity Nucleon operators from Table IV are dominant in the spectral overlaps. One of them has a quasi-local structure (indicated as  $S_5$  for no derivatives) with  $J = \frac{1}{2}$ , while the others involve two derivatives coupled either to  $L = 0, 1$ , or  $2$ , and are labeled as  $S_M$ ,  $P_A$  or  $D_5$  and  $D_M$ . We find that there is not a unique mapping of each state to one particular operator, rather each operator contributes in varying magnitude to each state, indicating significant mixing in this basis.

These results, along with the observation that the numbers of states are consistent with the numbers of non-relativistic operators in each  $J^+$ , suggest that this band of positive-parity states belongs to more than one  $SU(6) \otimes O(3)$  multiplet, with now mixing among the multiplets mentioned before; namely, the  $[70, 0^+]$ ,  $[56, 2^+]$ ,  $[70, 2^+]$   $[20, 1^+]$  and a radially excited  $[56, 0^+]$ . It is notable that there is overlap with all the allowed  $L_\pi J^P$  multiplets with  $L \leq 2$ , and in particular, there is mixing with the  $[20, 1^+]$  multiplet. There does not appear to be any “freezing” of degrees of freedom as suggested in some diquark models (for some reviews see Refs. [29, 30]). We will return to this point in the summary.

As we move up to the second excited negative-parity band in the Nucleon and Delta channels, we find the “non-relativistic”  $P_M$  operators discussed previously do not feature prominently in the spectral overlaps in these higher lying excited states. Instead, operators using two derivatives together with one quark having a lower component ( $\rho = -$ ) Dirac structure appear, some of which appear in Figures 3 and 4. The lower component spinor contributes a factor  $-1$  to the parity. Similarly, those operators that featured prominently in the first excited positive parity band do not appear significantly in the second excited positive band in the Nucleon and Delta channels. Instead, operators involving two derivatives and two lower-component Dirac spinors appear. The lower components effectively bring in angular momentum, but are not equivalent in spatial structure. To adequately resolve the internal structure of these higher lying states will require the introduction of operators featuring three and four derivatives.

## B. Quark mass dependence

At the two lighter pion masses,  $m_\pi = 444$  and  $396$  MeV, we find the spectra for Nucleons and Deltas, classified by irreps, to be qualitatively similar to the heaviest pion mass case. The spin identification techniques described above are successful, and the resulting spectrum, identified by spin is shown in Fig. 12 for the ensemble at



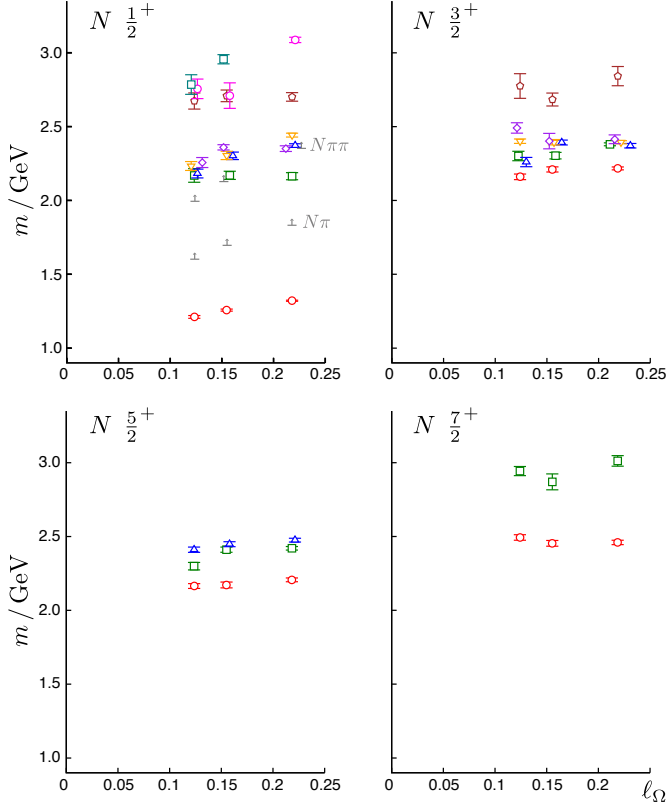


FIG. 14: Lightest few Nucleon  $J = \frac{1}{2}^+, \frac{3}{2}^+, \frac{5}{2}^+, \text{ and } \frac{7}{2}^+$  states. Also shown in  $N_{\frac{1}{2}}^+$  is the threshold for  $N\pi$  and  $N\pi\pi$ . The influence in the spectrum from these thresholds is complicated by the use of a finite spatial cubic box. Further discussion is in Section IX.

$m_\pi = 396$  MeV, normalized in units of the measured  $\Omega$  baryon mass determined at this quark mass.

The Nucleon and Delta spectrum is qualitatively similar to that determined at the heaviest pion mass - the  $m_\pi = 524$  MeV lattices - albeit typically at smaller mass in units of the  $\Omega$  baryon mass. There are the same number and pattern of low lying negative parity Nucleon and Delta states, as well as in the first excited band of positive parity states. Again, the low lying negative parity Delta states are slightly higher than the corresponding Nucleon states. There is a slightly enhanced splitting for the first excited band of positive parity Delta states across  $J^+$ , as well as more mixing among the positive parity Nucleon states around  $m/m_\Omega \sim 1.3$ .

In Figures 14 - 17, we show extracted state masses as a function of  $\ell_\Omega \equiv \frac{9}{4} \frac{(a_t m_\pi)^2}{(a_t m_\Omega)^2}$  which we use as a proxy for the quark mass [11] for the three quark masses listed in Table I. The state masses are presented via  $\frac{a_t m_H}{a_t m_\Omega} m_\Omega^{\text{phys}}$ . The ratio of the state mass ( $m_H$ ) to the  $\Omega$ -baryon mass computed on the same lattice removes the explicit scale dependence and multiplying by the physical  $\Omega$ -baryon mass conveniently expresses the result in MeV units. This is clearly not a unique scale-setting prescription, but

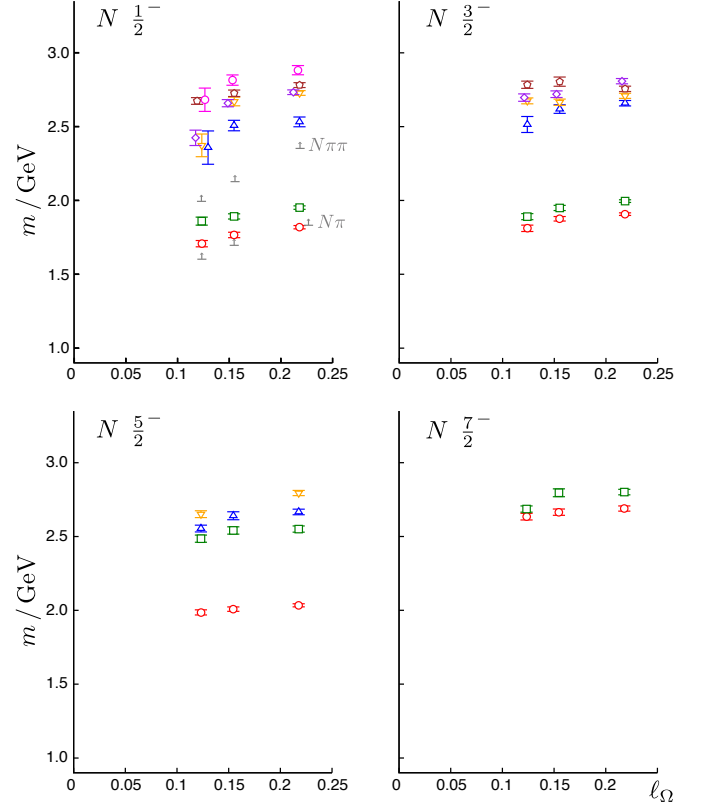


FIG. 15: Lightest few Nucleon  $J = \frac{1}{2}^-, \frac{3}{2}^-, \frac{5}{2}^-, \text{ and } \frac{7}{2}^-$  states. Also shown in  $N_{\frac{1}{2}}^-$  is the threshold for  $N\pi$  and  $N\pi\pi$ . The influence in the spectrum from these thresholds is complicated by the use of a finite spatial cubic box. Further discussion is in Section IX.

it serves to display the data in a relatively straightforward way. We remind the reader that the data between different quark masses are uncorrelated since they follow from computations on independently generated dynamical gauge-fields.

In Figure 14 we show the mass of some of the lowest identified positive parity levels. In Figure 15 we show the lowest few negative parity Nucleon levels. To help resolve near degeneracies, we slightly shift symbols at the same pion mass horizontally in  $\ell_\Omega$ . In some cases, for comparison, we plot the mass of the lightest  $N\pi$  and  $N\pi\pi$  thresholds - the mass follows from the simple sum of the extracted masses on these lattices. In general, the lattice levels decrease with the quark mass. There is no observed dramatic behavior, for example, from crossing of thresholds.

Notable in these plots is the clustering of bands of levels as seen in Figures 11 and 12 and described above. In the first excited positive parity Nucleon band, there is a tendency for the levels across  $J^+$  to cluster, and is most readily apparent in the  $J = \frac{1}{2}^+$  to cluster around  $m/m_\Omega \sim 1.3$  as the pion mass decreases. Another notable feature in these figures is the absence of an excited Nucleon  $J = \frac{1}{2}^+$  state comparable, or slightly below, the

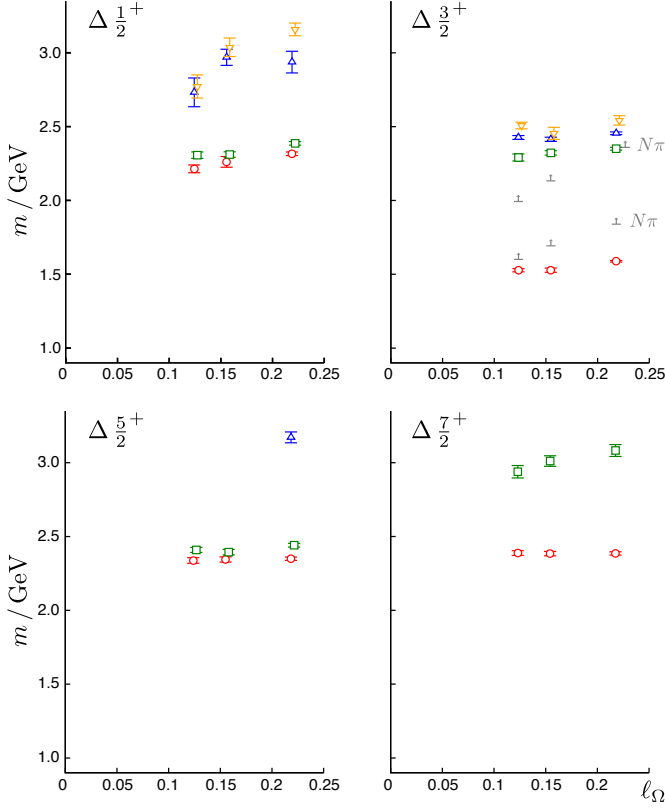


FIG. 16: Lightest few Delta  $J = \frac{1}{2}^+, \frac{3}{2}^+, \frac{5}{2}^+$ , and  $\frac{7}{2}^+$  states. Also shown in  $\Delta_{\frac{3}{2}^+}$  is the threshold for  $N\pi$  and  $N\pi\pi$ . The influence in the spectrum from these thresholds is complicated by the use of a finite spatial cubic box. Further discussion is in Section IX.

lowest lying  $\frac{1}{2}^-$  level as reported in the PDG [31]. Similarly, there is no low lying Delta  $J = \frac{3}{2}^+$  state comparable in mass to the  $\frac{3}{2}^-$ . The ordering of the low-lying states in the Nucleon spectrum, and in particular the spectrum of the  $N_{\frac{1}{2}^+}$  channel, has been the subject of much effort in lattice QCD.

### C. Comparisons

In Figure 18, we show a comparison of our result for the Nucleon  $J = \frac{1}{2}^+$  spectrum with other calculations in full QCD. Those shown in grey are from Ref. [32] using  $2 \oplus 1$  dynamical quark flavors, while those in orange are from Ref. [4] using two dynamical light-quark flavors. Each of these calculations employs a different means to set the lattice scale, and we have made no attempt to resolve these calculations to a common scale-setting scheme. Rather our aim in this discussion is to compare the pattern of states that has emerged in each calculation, and to provide a possible explanation for the differences.

References [32] and [4] find only two excited levels be-

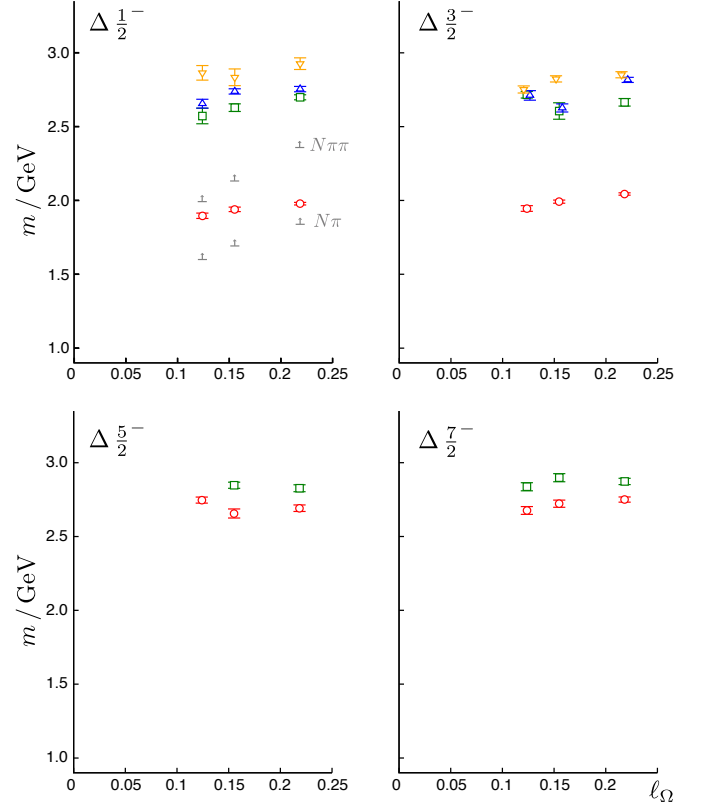


FIG. 17: Lightest few Delta  $J = \frac{1}{2}^-, \frac{3}{2}^-, \frac{5}{2}^-$ , and  $\frac{7}{2}^-$  states. Also shown in  $\Delta_{\frac{1}{2}^-}$  is the threshold for  $N\pi$  and  $N\pi\pi$ . The influence in the spectrum from these thresholds is complicated by the use of a finite spatial cubic box. Further discussion is in Section IX.

low 2.8 GeV, notably isolated from one another in the case of Ref. [32], at pion masses comparable to those in this study. At the lightest quark mass reported in this work, there are *four* nearly degenerate excited states found at approximately 2.2 GeV, and three nearly degenerate states near 2.8 GeV. A possible explanation for the discrepancy in the number of levels is the operator constructions used. Refs. [4, 32] use a basis of local or quasi-local operators, without, for example, derivatives, but with multiple smearing radii. These operators, which have an  $S$ -wave spatial structure concentrated at the origin, can have overlap with radial excitations of  $S$ -waves, but will have limited overlap with higher orbital waves. The results presented here suggest the observed excited  $J = \frac{1}{2}^+$  states are admixtures of radial excitations as well as  $D$ -wave and anti-symmetric  $P$ -waves structures, and the inclusion of operators featuring such structures is essential to resolve the degeneracy of states. The impact of an incomplete basis of operators will be addressed more in Section IX.

The authors of Ref. [32] note the large drop in the energies of the first and second excited states at their lightest pion mass, and ascribe this to the emergence of a light “Roper” in their calculation. While we do not reach cor-



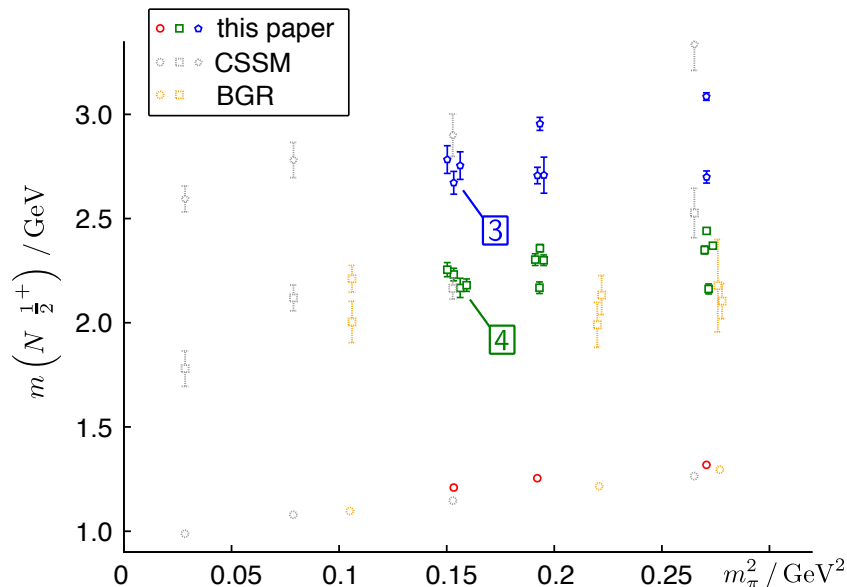


FIG. 18: Comparison of results for the Nucleon  $J = \frac{1}{2}^+$  channel. The results shown in grey are from Ref. [32], while those in orange are from Ref. [4]. Note that data are plotted using the scale-setting scheme in the respective papers. Results from this paper are shown in red (the ground state), green and blue. At the lightest pion mass, there is a clustering of four states as indicated near 2 GeV, while there are three nearly degenerate states 2.7 GeV. Operators featuring the derivative constructions discussed in this paper feature prominently in these excited states.

respondingly light pion masses and large volumes in this study, the work presented here clearly shows the need for a sufficiently complete basis of operators before a faithful description of the spectrum can emerge, and the identification of the Roper resonance be warranted. Indeed, even our work remains incomplete since we have entered a regime of open decay channels, discussed next, requiring the addition of multi-particle operators to the basis.

## IX. MULTI-PARTICLE STATES

In the previous section we presented the extracted spectra from calculations with three different light quark masses. In each case we were able, using the operator overlaps, to match states across irreps that we believe are subduced from the same continuum spin state. This suggests an interpretation of the spectrum in terms of single-hadron states, while in principle our correlators should receive contributions from all eigenstates of finite-volume QCD having the appropriate quantum numbers. This includes baryon-meson states which in finite volume have a discrete spectrum. Where are these multi-particle states?

This issue was investigated in the meson sector [17] where the spectrum was compared between multiple volumes and on multiple mass data sets. In particular, under change of volume, the extracted spectrum did not resemble the changing pattern of levels one would expect from two-meson states, but rather was largely volume-

independent. As such, the interpretation of the observed levels was that of a single particle spectrum. In this work, some initial investigations were made with a  $20^3 \times 128$  lattice at the lightest pion mass available, and similar observations are made; namely, the spectrum between different volumes does not change substantially. We are thus led to interpret the spectrum in terms of single hadron states. The subsequent observations we make are quite similar to those made for mesons [17].

The overlap of a localized three-quark operator onto a baryon-meson state will be suppressed by  $1/\sqrt{V}$ , where  $V$  is the lattice volume, if the operator creates a resonance with a finite width in the infinite volume limit. This fall-off is matched by a growth in the density of states with the volume and the resonant state thus maintains a finite width as the mixing with each discrete state falls. The simulations in this study are carried out in cubic volumes with side-lengths  $\sim 2$  fm, which might be sufficiently large that the mixing between one of the low-lying two-particle states and a resonance is suppressed sufficiently for it to be undetectable with the three-quark operator basis.

Even if the mixing between localized single-hadron states and baryon-meson states to form resonance-like finite volume eigenstates is not small, there still remains a practical difficulty associated with using only three-quark operators. In this case the state can be produced at the source time-slice through its localized single-hadron component, while the correlator time dependence obtained from  $e^{-Ht}$  will indicate the mass of the resonant eigen-

state. Consider a hypothetical situation in which a single baryon-meson state, denoted by  $|2\rangle$ , mixes arbitrarily strongly with a single localized single-hadron state,  $|1\rangle$ , with all other states being sufficiently distant in energy as to be negligible. There will be two eigenstates

$$\begin{aligned} |a\rangle &= \cos\theta|1\rangle + \sin\theta|2\rangle \\ |b\rangle &= -\sin\theta|1\rangle + \cos\theta|2\rangle, \end{aligned}$$

with masses  $m_a, m_b$ . At the source (and sink) only the localized single-hadron component of each state overlaps with the operators in our basis and hence the overlaps,  $Z_i^{a,b} \equiv \langle a, b | \mathcal{O}_i^\dagger | 0 \rangle$ , will differ only by an overall multiplicative constant,  $Z_i^a = \cos\theta Z_i^{(1)}$ ,  $Z_i^b = -\sin\theta Z_i^{(1)}$ . As such the eigenvectors  $v^a, v^b$  point in the same direction and cannot be made orthogonal. Thus the time dependence of both states will appear in the *same* principal correlator as

$$\lambda(t) \sim A_a e^{-m_a(t-t_0)} + A_b e^{-m_b(t-t_0)} + \dots$$

Since  $m_a$  and  $m_b$  most likely do not differ significantly (on the scale of  $a_t^{-1}$ ) it will prove very difficult to extract a clear signal of two-exponential behavior from the principal correlator. This is precisely why the variational method's orthogonality condition on near degenerate states is so useful, but we see that it cannot work here and we are left trying to extract two nearby states from a  $\chi^2$  fit to time-dependence. Typically this is not possible and reasonable looking fits to data are obtained with just one low-mass exponential. This is analogous to the interpretation made in the comparison between our computed  $N_{\frac{1}{2}}^+$  spectrum, and those computed using only rotationally-symmetric smeared (quasi-)local sources[4, 32], shown in Figure 18; our results showed a cluster of four near-degenerate states, while the other analyses showed one or perhaps two since all four states would only couple through their  $S$ -wave components.

Thus, in some portions of the extracted spectrum, we might be observing admixtures of “single-particle” and baryon-meson states. A conservative interpretation then of our spectrum is that the mass values are only accurate up to the hadronic width of the state extracted, since this width is correlated with mixing with baryon-meson states via a scattering phase-shift.

In order to truly compare with the experimental situation, we would like to explicitly observe resonant behavior, thus to obtain a significant overlap with multi-hadron states, we should include operators with a larger number of fermion fields into our basis, and in particular, multi-particle operators. The construction of single-meson and single baryon operators of definite continuum helicity and subduced into the ‘in flight’ little-group irreps can be done using the tables in [33, 34]. Spin identification is possible and will be reported in future work. These in-flight operators can be used in two-particle constructions, and along with single particle operators, provide a far more complete determination of the excited levels in an irrep.

As shown by Lüscher[35], one can map these discrete energy levels onto the the continuum energy dependent phase shift within a partial wave expansion, including the phase shift for higher partial waves. Such a technique was recently used to determine the  $L = 0$  and  $L = 2$  phase shift for non-resonant  $I = 2$   $\pi\pi$  scattering [36]. The mapping of the phase shift is both volume and irrep dependent. This is the origin of the cautionary remarks in the captions of Figures 14 - 17. Namely, the location of the threshold energies are in fact irrep dependent and not solely determined by the energy of the continuum states.

With suitable understanding of the discrete energy spectrum of the system, the Lüscher formalism can be used to extract the energy dependent phase shift for a resonant system, such as has been performed for the  $I = 1$   $\rho$  system [37]. The energy of the resonant state is determined from the energy dependence of the phase shift. It is this resonant energy that is suitable for chiral extrapolations.

Annihilation dynamics feature prominently in resonant systems, and these dynamics arise from quark disconnected diagrams in multi-particle constructions. Utilizing the techniques developed recently for the study of isoscalar systems[38], distillation, and stochastic variants [25], can be used for the efficient numerical evaluation of multi-particle systems.

## X. SUMMARY

We have described in detail our method for extracting a large number of Nucleon and Delta excited states using the variational method on dynamical anisotropic lattices. Key to the success of the method has been the use of a large basis of carefully constructed operators, namely all three quark baryon operators consistent with classical continuum symmetries, and with up to two derivatives, that are subsequently projected onto the irreducible representations of the cubic group. We have exploited the observed approximate realization of rotational symmetry to devise a method of spin identification based on operator overlaps, enabling us to confidently assign continuum spin quantum numbers to many states. We have demonstrated the importance of having a suitable operator basis with overlap to all the continuum spin states that contribute to the spectrum. We have then demonstrated the stability of the spectra with respect to changing the number of distillation vectors and the details of the variational analysis. We have successfully applied these techniques at one lattice volume with three different light quark masses. We are able to reliably extract a large number of excited states with  $J^P$  ranging from  $J = \frac{1}{2}$  up through  $J = \frac{7}{2}$  in both positive and negative parity. These are the first lattice calculations to achieve such a resolution of states in the baryon sector with spin assignments and  $J \geq \frac{5}{2}$ .

We find a high multiplicity of levels spanning across  $J^P$

which is consistent with  $SU(6) \otimes O(3)$  multiplet counting, and hence with that of the non-relativistic  $qqq$  constituent quark model. In particular, the counting of levels in the low lying negative parity sectors are consistent with the non-relativistic quark model and with the observed experimental states [31]. The spectrum observed in the first excited positive parity sector is also consistent in counting with the quark model, but the comparison with experiment is less clear with the quark model predicting more states than are observed experimentally, spurring phenomenological investigations to explain the discrepancies (e.g., see Refs. [27, 29–31, 39–41]).

We find that each of the operators in our basis features prominently in some energy level, and there is significant mixing among each of the allowed multiplets, including the **20**-plet that is present in the non-relativistic  $qqq$  quark model, but does not appear in quark-diquark models[29], and in particular Ref. [42]. This adds further credence to the assertion that there is no “freezing” of degrees of freedom with respect to those of the non-relativistic quark model. These qualitative features of the calculated spectrum extend across all three of our quark-mass ensembles. Furthermore, we see no evidence for the emergence of parity-doubling in the spectrum[28].

We have argued that the extracted spectrum can be interpreted in terms of single-hadron states, and based on investigations in the meson sector[17] and initial investigations of the baryon sector at a larger volume, we find little evidence for multi-hadron states. To study multi-particle states, and hence the resonant nature of excited states, we need to construct operators with a larger number of fermion fields. Such constructions are in progress, and we believe that the addition of these operators will lead to a denser spectrum of states which can

be interpreted in terms of resonances via techniques like Lüscher’s and its inelastic extensions[43].

The extraction and identification of a highly excited, spin identified single-hadron spectrum, represents an important step towards a determination of the excited baryon spectrum. The calculation of the single-baryon spectrum including strange quarks is ongoing. Combining the methods developed in this paper with finite volume techniques for the extraction of phase shifts, future work will focus on the determination of hadronic resonances within QCD.

### Acknowledgments

We thank our colleagues within the Hadron Spectrum Collaboration. We also acknowledge illuminating discussions with Simon Capstick and Winston Roberts. **Chroma** [44] and **QUDA** [45, 46] were used to perform this work on clusters at Jefferson Laboratory under the USQCD Initiative and the LQCD ARRA project. Gauge configurations were generated using resources awarded from the U.S. Department of Energy INCITE program at Oak Ridge National Lab, the NSF Teragrid at the Texas Advanced Computer Center and the Pittsburgh Supercomputer Center, as well as at Jefferson Lab. SJW acknowledges support from U.S. Department of Energy contract DE-FG02-93ER-40762. RGE, JJD and DGR acknowledge support from U.S. Department of Energy contract DE-AC05-06OR23177, under which Jefferson Science Associates, LLC, manages and operates Jefferson Laboratory.

- 
- [1] C. Hoelbling, PoS **LATTICE2010**, 011 (2010), 1102.0410.
  - [2] M. Mahbub, W. Kamleh, D. B. Leinweber, A. O Cais, and A. G. Williams, Phys.Lett. **B693**, 351 (2010), 1007.4871.
  - [3] M. Mahbub, A. O. Cais, W. Kamleh, D. B. Leinweber, and A. G. Williams, Phys.Rev. **D82**, 094504 (2010), 1004.5455.
  - [4] G. P. Engel, C. Lang, M. Limmer, D. Mohler, and A. Schafer (BGR [Bern-Graz-Regensburg] Collaboration), Phys.Rev. **D82**, 034505 (2010), 1005.1748.
  - [5] N. Mathur, Y. Chen, S. Dong, T. Draper, I. Horvath, et al., Phys.Lett. **B605**, 137 (2005), hep-ph/0306199.
  - [6] S. Basak et al. (Lattice Hadron Physics (LHPC)), Phys. Rev. **D72**, 074501 (2005), hep-lat/0508018.
  - [7] S. Basak et al., Phys. Rev. **D72**, 094506 (2005), hep-lat/0506029.
  - [8] S. Basak et al., Phys. Rev. **D76**, 074504 (2007), arXiv:0709.0008.
  - [9] J. M. Bulava et al., Phys. Rev. **D79**, 034505 (2009), arXiv:0901.0027.
  - [10] R. G. Edwards, B. Joo, and H.-W. Lin, Phys. Rev. **D78**, 054501 (2008), arXiv:0803.3960.
  - [11] H.-W. Lin et al. (Hadron Spectrum), Phys. Rev. **D79**, 034502 (2009), arXiv:0810.3588.
  - [12] C. Michael, Nucl. Phys. **B259**, 58 (1985).
  - [13] M. Luscher and U. Wolff, Nucl. Phys. **B339**, 222 (1990).
  - [14] B. Blossier, M. Della Morte, G. von Hippel, T. Mendes, and R. Sommer, JHEP **04**, 094 (2009), 0902.1265.
  - [15] J. Bulava et al., Phys. Rev. **D82**, 014507 (2010), 1004.5072.
  - [16] J. J. Dudek, R. G. Edwards, M. J. Peardon, D. G. Richards, and C. E. Thomas, Phys. Rev. Lett. **103**, 262001 (2009), 0909.0200.
  - [17] J. J. Dudek et al., Phys. Rev. **D82**, 034508 (2010), 1004.4930.
  - [18] C. Morningstar and M. J. Peardon, Phys. Rev. **D69**, 054501 (2004), hep-lat/0311018.
  - [19] M. Peardon et al. (Hadron Spectrum), Phys. Rev. **D80**, 054506 (2009), 0905.2160.
  - [20] T. Burch, C. Hagen, M. Hetzenegger, and A. Schafer, Phys. Rev. **D79**, 114503 (2009), 0903.2358.
  - [21] C. Gatttringer, L. Y. Glozman, C. B. Lang, D. Mohler, and S. Prelovsek, Phys. Rev. **D78**, 034501 (2008),

- 0802.2020.
- [22] T. Burch et al., Phys. Rev. **D73**, 094505 (2006), hep-lat/0601026.
  - [23] T. Burch et al. (Bern-Graz-Regensburg), Phys. Rev. **D70**, 054502 (2004), hep-lat/0405006.
  - [24] J. J. Dudek, R. G. Edwards, N. Mathur, and D. G. Richards, Phys. Rev. **D77**, 034501 (2008), arXiv:0707.4162.
  - [25] C. Morningstar, J. Bulava, J. Foley, K. J. Juge, D. Lenkner, et al., Phys.Rev. **D83**, 114505 (2011), 1104.3870.
  - [26] N. Isgur and G. Karl, Phys. Rev. **D18**, 4187 (1978).
  - [27] N. Isgur and G. Karl, Phys. Rev. **D19**, 2653 (1979).
  - [28] L. Glozman, Phys.Lett. **B475**, 329 (2000), hep-ph/9908207.
  - [29] M. Anselmino, E. Predazzi, S. Ekelin, S. Fredriksson, and D. B. Lichtenberg, Rev. Mod. Phys. **65**, 1199 (1993).
  - [30] S. Capstick and W. Roberts, Prog. Part. Nucl. Phys. **45**, S241 (2000), nucl-th/0008028.
  - [31] K. Nakamura et al. (Particle Data Group), J. Phys. **G37**, 075021 (2010).
  - [32] M. S. Mahbub, W. Kamleh, D. B. Leinweber, P. J. Moran, and A. G. Williams (2010), 1011.5724.
  - [33] D. C. Moore and G. T. Fleming, Phys. Rev. **D73**, 014504 (2006), hep-lat/0507018.
  - [34] D. C. Moore and G. T. Fleming, Phys. Rev. **D74**, 054504 (2006), hep-lat/0607004.
  - [35] M. Luscher, Nucl. Phys. **B364**, 237 (1991).
  - [36] J. J. Dudek, R. G. Edwards, M. J. Peardon, D. G. Richards, and C. E. Thomas, Phys.Rev. **D83**, 071504 (2011), 1011.6352.
  - [37] X. Feng, K. Jansen, and D. B. Renner, Phys.Rev. **D83**, 094505 (2011), 1011.5288.
  - [38] J. J. Dudek, R. G. Edwards, B. Joo, M. J. Peardon, D. G. Richards, et al., Phys.Rev. **D83**, 111502 (2011), 1102.4299.
  - [39] S. Capstick and N. Isgur, Phys. Rev. **D34**, 2809 (1986).
  - [40] L. Y. Glozman and D. O. Riska, Phys. Rept. **268**, 263 (1996), hep-ph/9505422.
  - [41] J. L. Goity, C. Schat, and N. N. Scoccola, Phys. Lett. **B564**, 83 (2003), hep-ph/0304167.
  - [42] D. B. Lichtenberg and L. J. Tassie, Phys. Rev. **155**, 1601 (1967).
  - [43] M. Lage, U.-G. Meissner, and A. Rusetsky, Phys. Lett. **B681**, 439 (2009), 0905.0069.
  - [44] R. G. Edwards and B. Joo, Nucl. Phys. B. Proc. Suppl. **140**, 832 (2005).
  - [45] M. A. Clark et al., Comput. Phys. Commun. **181**, 1517 (2010), 0911.3191.
  - [46] R. Babich, M. A. Clark, and B. Joo (2010), 1011.0024.

## Appendix A: Construction of flavor/spin/space symmetric states

Consider the construction of sets of definite symmetry for three objects that can be labeled by  $x$ ,  $y$ , and  $z$ , where the first object is labeled by  $x$ , the second is labeled by  $y$  and the third is labeled by  $z$ . There are in general, four definite symmetry combinations: symmetric, mixed-symmetric, mixed anti-symmetric, and totally antisymmetric, denoted by  $S$ ,  $MS$ ,  $MA$ ,  $A$ .

Let symmetry projection operator  $S_{\Sigma} \begin{pmatrix} x & y & z \\ x' & y' & z' \end{pmatrix}$  be defined so that its action on a generic object with labels  $x'$ ,  $y'$  and  $z'$  is to create a superposition of objects, denoted by  $\{xyz\}_{\Sigma}$ , with symmetry  $\Sigma$  of their labels as follows,

$$\{xyz\}_{\Sigma} = \sum_{x'y'z'} S_{\Sigma} \begin{pmatrix} x & y & z \\ x' & y' & z' \end{pmatrix} \{x'y'z'\}. \quad (A1)$$

Permutation operators  $S_{\Sigma}$  can be inferred from their action on an object with three labels to produce the four allowed symmetry combinations as follows,

$$\begin{aligned} \{xyz\}_S &= N_S [\{xyz\} + \{yxz\} + \{zyx\} + \{yzx\} \\ &\quad + \{xzy\} + \{zxy\}], \\ \{xyz\}_{MS} &= N_{MS} [\{xyz\} + \{yxz\} + \{zyx\} + \{yzx\} \\ &\quad - 2\{xzy\} - 2\{zxy\}], \\ \{xyz\}_{MA} &= N_{MA} [\{xyz\} - \{yxz\} + \{zyx\} - \{yzx\}], \\ \{xyz\}_A &= N_A [-\{xyz\} + \{xzy\} - \{yzx\} + \{yxz\} \\ &\quad - \{zxy\} + \{zyx\}]. \end{aligned} \quad (A2)$$

If two or more labels are the same, then equivalent terms must be combined and the normalization constants adjusted to give an appropriate normalization, e.g., for orthonormal quantum states  $N_S = \frac{1}{\sqrt{6}}$  when  $x$ ,  $y$  and  $z$  all are different. By convention, mixed symmetries are  $MS$  or  $MA$  according to whether the first two labels are symmetric or antisymmetric.

The use of projection operators allows the same constructions to be applied to the labels of operators as are applied to the labels of the states created by the operators. They also provide the basis for a straightforward computational algorithm that yields the desired superpositions.

Baryon operators have sets of labels for flavor, spin, and spatial arguments that transform independently, therefore as direct products. Each of these sets of labels can be arranged according to Eq. (A2). Then the symmetries of the sets of flavor labels must be combined with the symmetries of the sets of spin and spatial labels in order to make an overall symmetric object as discussed in the text. The general rules for combining direct products of objects with independent labels sets 1 and 2 to

make overall symmetries of the combined sets of all labels, denoted by 1,2, are as follows,

$$\begin{aligned} \{1\}_S\{2\}_S &= \{1,2\}_S, & \{1\}_S\{2\}_{MS} &= \{1,2\}_{MS}, \\ \{1\}_S\{2\}_{MA} &= \{1,2\}_{MA}, & \{1\}_S\{2\}_A &= \{1,2\}_A, \\ \{1\}_A\{2\}_S &= \{1,2\}_A, & \{1\}_A\{2\}_{MS} &= \{1,2\}_{MA}, \\ -\{1\}_A\{2\}_{MA} &= \{1,2\}_{MS}, & \{1\}_A\{2\}_A &= \{1,2\}_S, \end{aligned}$$

$$\begin{aligned} \frac{1}{\sqrt{2}}(+\{1\}_{MS}\{2\}_{MS} + \{1\}_{MA}\{2\}_{MA}) &= \{1,2\}_S, \\ \frac{1}{\sqrt{2}}(-\{1\}_{MS}\{2\}_{MS} + \{1\}_{MA}\{2\}_{MA}) &= \{1,2\}_{MS}, \\ \frac{1}{\sqrt{2}}(+\{1\}_{MS}\{2\}_{MA} + \{1\}_{MA}\{2\}_{MS}) &= \{1,2\}_{MA}, \\ \frac{1}{\sqrt{2}}(-\{1\}_{MS}\{2\}_{MA} + \{1\}_{MA}\{2\}_{MS}) &= \{1,2\}_A \end{aligned} \quad (A3)$$

### 1. Dirac spin

The construction of Dirac spin representations follows Table 14 in Appendix B of Ref. [7]. A Dirac spinor with an index that takes four values is formed from direct products of two spinors that have indices that take two values: one for ordinary spin ( $s$ -spin) and the other for intrinsic parity ( $\rho$ -spin). The  $s$ -spin indices are  $s = +$  for spin up and  $s = -$  for spin down while the  $\rho$ -spin indices are  $\rho = +$  for positive intrinsic parity and  $\rho = -$  for negative intrinsic parity. These  $\rho$ - and  $s$ -spin indices determine the Dirac spin index (in the rest frame) as shown in Table V, based on the Dirac-Pauli representation of Dirac matrices.

There are eight  $s$ -spin states for a three-quark baryon and they are obtained by projecting an arbitrary state to combinations with good symmetry. The resulting states follow from Eq. (A2) with  $x, y$  and  $z$  taking two values,  $+$  and  $-$ , which produces four symmetric (S) states with total spin  $\frac{3}{2}$ ,

$$\begin{aligned} \left|\frac{3}{2}, +\frac{3}{2}\right\rangle_S &= |+++ \rangle_S, \\ \left|\frac{3}{2}, +\frac{1}{2}\right\rangle_S &= |++- \rangle_S, \\ \left|\frac{3}{2}, -\frac{1}{2}\right\rangle_S &= |+- - \rangle_S, \\ \left|\frac{3}{2}, -\frac{3}{2}\right\rangle_S &= |-- - \rangle_S, \end{aligned} \quad (A4)$$

two mixed-symmetric (MS) states with total spin  $\frac{1}{2}$ ,

$$\begin{aligned} \left|\frac{1}{2}, +\frac{1}{2}\right\rangle_{MS} &= +|+-+ \rangle_{MS}, \\ \left|\frac{1}{2}, -\frac{1}{2}\right\rangle_{MS} &= -|-+- \rangle_{MS}, \end{aligned} \quad (A5)$$

and two mixed-antisymmetric (MA) states with total spin  $\frac{1}{2}$ ,

$$\begin{aligned} \left|\frac{1}{2}, +\frac{1}{2}\right\rangle_{MA} &= +|+-+ \rangle_{MA}, \\ \left|\frac{1}{2}, -\frac{1}{2}\right\rangle_{MA} &= -|-+- \rangle_{MA}. \end{aligned} \quad (A6)$$

Dirac	$\rho$	$s$
1	+	+
2	+	-
3	-	+
4	-	-

TABLE V: Mapping of Dirac spin indices to  $\rho$  and  $s$  labels.

The states on the right side are normalized states of definite symmetry. The eight  $\rho$ -spin states take exactly the same form as the  $s$ -spin states.

The 64 Dirac spin labels of three quarks are obtained from direct products of  $\rho$ -spin and  $s$ -spin states of the quarks. The possible symmetries of the Dirac spinors are obtained from the multiplication rules in Eq. A3, together with Table V, which shows how each quark's Dirac index is determined by its  $s$ -spin and  $\rho$ -spin indices. Examples of the construction are given in Ref. [7]. Equal numbers of positive- and negative-parity states are always produced. The octahedral irrep of the product is  $G_1$  for  $s$ -spin  $\frac{1}{2}$  and  $H$  for  $s$ -spin  $\frac{3}{2}$  representations of  $SU(2)$ . Table VI shows the irreps of  $SU(2)$  that are produced. The number of embeddings of each irrep also is listed. Parities of the states are determined by products of the  $\rho$ -spins of the three quarks.

### 2. Flavor

The flavor states with well-defined symmetries also are constructed using Eq. (A2). For the purposes of discussion, we will consider the flavor symmetric limit, i.e., degenerate quark masses. There are three separate representations – the symmetric (S) states are the  $SU(3)$  decuplet,  $|10\rangle_S$ , the mixed-symmetric (MS, MA) states are the  $SU(3)$  octets,  $|8\rangle_{MS,MA}$ , and the antisymmetric (A) state is the  $SU(3)$  flavor-singlet state,  $|1\rangle_A$ . The  $\Delta^+$  is  $|udu\rangle_S$ , while the proton is  $|udu\rangle_{MA,MS}$ . The  $\Sigma^0$  is  $|uds\rangle_{MA,MS}$ . The octet, singlet and decuplet constructions are shown in Table VII.

Within the  $SU(3)$  flavor representations, we also have  $SU(2)$  isospin states. In the construction that follows, it is straightforward to generalize to the case of broken  $SU(3)$ . The combinations of symmetry states remain valid, however, there are some new states, such as  $\Sigma$  in a S flavor state.

### 3. Orbital angular momentum based on covariant derivatives

Smearing of quark fields is based on the distillation method of Ref. [19]. It is used in order to filter out the effects of small scale fluctuations of the gauge fields and it provides a spherically symmetric distribution of each

Dirac	IR	Emb	$\rho \otimes s$	
S	$\frac{1}{2}$	1	$\frac{1}{\sqrt{2}} ( +  \rho\rangle_{\text{MS}}  s\rangle_{\text{MS}} +  \rho\rangle_{\text{MA}}  s\rangle_{\text{MA}} )$	
	$\frac{3}{2}$	1, 2	$ \rho\rangle_s  s\rangle_s$	
M	$\frac{1}{2}$	1, 2	MS	$ \rho\rangle_s  s\rangle_{\text{MS}}$
		3		$\frac{1}{\sqrt{2}} ( -  \rho\rangle_{\text{MS}}  s\rangle_{\text{MS}} +  \rho\rangle_{\text{MA}}  s\rangle_{\text{MA}} )$
	$\frac{3}{2}$	1		$ \rho\rangle_{\text{MS}}  s\rangle_s$
			MA	$ \rho\rangle_s  s\rangle_{\text{MA}}$
				$\frac{1}{\sqrt{2}} ( +  \rho\rangle_{\text{MS}}  s\rangle_{\text{MA}} +  \rho\rangle_{\text{MA}}  s\rangle_{\text{MS}} )$
				$ \rho\rangle_{\text{MA}}  s\rangle_s$
A	$\frac{1}{2}$	1	$\frac{1}{\sqrt{2}} ( -  \rho\rangle_{\text{MS}}  s\rangle_{\text{MA}} +  \rho\rangle_{\text{MA}}  s\rangle_{\text{MS}} )$	

TABLE VI: Symmetries of Dirac spin states based on direct products of  $\rho$ -spin and  $s$ -spin states for three quarks. States labeled as  $|\rho\rangle_{\Sigma}$  refer to a  $\rho$ -spin state with symmetry  $\Sigma$  from Eqs. (A4-A6). Similarly, states labeled as  $|s\rangle_{\Sigma}$  refer to a  $s$ -spin state with symmetry  $\Sigma$  from Eqs. (A4-A6). Direct products of the  $\rho$ -spin and  $s$ -spin states yield sums of three-quark terms in which each quark has a  $\rho$  and  $s$  label. That determines each quark's Dirac index according to Table V.

Octet, 8					Decuplet, 10				
	$I$	$I_z$	$S$	$\phi_{\text{MS}}$	$\phi_{\text{MA}}$		$I$	$I_z$	$S$
$p$	$\frac{1}{2}$	$+\frac{1}{2}$	0	$ udu\rangle_{\text{MS}}$	$ udu\rangle_{\text{MA}}$	$\Delta^{++}$	$\frac{3}{2}$	$+\frac{3}{2}$	0
$n$	$\frac{1}{2}$	$-\frac{1}{2}$	0	$- dud\rangle_{\text{MS}}$	$- dud\rangle_{\text{MA}}$	$\Delta^+$	$\frac{3}{2}$	$+\frac{1}{2}$	0
$\Lambda_8$	0	0	-1	$\frac{1}{\sqrt{2}} ( sud\rangle_{\text{MS}} -  uds\rangle_{\text{MS}})$	$\frac{1}{\sqrt{2}} ( sud\rangle_{\text{MA}} -  uds\rangle_{\text{MA}})$	$\Delta^0$	$\frac{3}{2}$	$-\frac{1}{2}$	0
$\Sigma_8^+$	1	+1	-1	$ usu\rangle_{\text{MS}}$	$ usu\rangle_{\text{MA}}$	$\Delta^-$	$\frac{3}{2}$	$-\frac{3}{2}$	0
$\Sigma_8^0$	1	0	-1	$ usd\rangle_{\text{MS}}$	$ usd\rangle_{\text{MA}}$	$\Sigma_{10}^+$	1	+1	-1
$\Sigma_8^-$	1	-1	-1	$ dsd\rangle_{\text{MS}}$	$ dsd\rangle_{\text{MA}}$	$\Sigma_{10}^0$	1	0	-1
$\Xi_8^0$	$\frac{1}{2}$	$+\frac{1}{2}$	-2	$- sus\rangle_{\text{MS}}$	$- sus\rangle_{\text{MA}}$	$\Sigma_{10}^-$	1	-1	-1
$\Xi_8^-$	$\frac{1}{2}$	$-\frac{1}{2}$	-2	$- sds\rangle_{\text{MS}}$	$- sds\rangle_{\text{MA}}$	$\Xi_{10}^0$	$\frac{1}{2}$	$+\frac{1}{2}$	-2
						$\Xi_{10}^-$	$\frac{1}{2}$	$-\frac{1}{2}$	-2
						$\Omega^-$	0	0	-3

Singlet, 1				
	$I$	$I_z$	$S$	$\phi_A$
$\Lambda_1^0$	0	0	-1	$ dus\rangle_A$

TABLE VII: Flavor octet, decuplet and singlet constructions.

quark field that carries no orbital angular momentum. In order to obtain higher spins, it is necessary to add spatial structure using covariant derivative operators, as described in the text, which are combined in definite symmetries that correspond to orbital angular momenta in the continuum. For a single derivative, ( $D^{[1]}$ ), the two symmetry combinations are given in Eq. (8), while for two derivatives, ( $D^{[2]}$ ), the combinations are given in Eq. (12).

Operators that have good spin in the continuum are built by applying some number of derivatives to the Dirac spinors. Using the  $SU(2)$  Clebsch-Gordan coefficients to combine orbital and spin angular momenta, the one-derivative operators are,

$$\left( D^{[1]} \Psi^{[S]} \right)^{[J,M]} = \sum_{m,s} \langle 1, m; S, s | J, M \rangle \vec{D}_{L=1,m}^{[1]} \Psi^{S,s}, \quad (\text{A7})$$

where  $S = \frac{1}{2}$  or  $\frac{3}{2}$  are the possible spin states of three quarks in the absence of derivatives. Reference [7] developed single derivative operators for baryons and it provides some examples of the incorporation of combinations of covariant derivatives into three-quark operators.

Additional derivatives together with  $SU(2)$  Clebsch-Gordan coefficients are used to obtain higher  $J$  states. For example, the two-derivative operators are first com-

bined to get  $L = 2$ ,

$$D_{L=2,M}^{[2]} = \sum_{m_1, m_2} \langle 1, m_1; 1, m_2 | 2, M \rangle D_{m_1}^{[1]} D_{m_2}^{[1]}. \quad (\text{A8})$$

This  $L = 2$  derivative operator is then applied to a spinor  $\Psi^{S,s}$  as follows,

$$\left( D_{L=2}^{[2]} \Psi^{[S]} \right)^{[J,M]} = \sum_{m,s} \langle 2, m; S, s | J, M \rangle D_{L=2,M}^{[2]} \Psi^{S,s}. \quad (\text{A9})$$

Derivative operator constructions for singlet, octet and decuplet follow from Table VIII. The single-site operators are symmetric in space, flavor and Dirac indices. With one derivative, a mixed symmetry flavor and spin construction is combined with mixed symmetry derivative operators to make the overall symmetric combinations. Similarly, with two derivatives, various spin-flavor symmetry states are combined with the derivative operators to make overall symmetric operators.

As noted above, three quarks with no derivatives can form at most spin  $\frac{1}{2}$  and  $\frac{3}{2}$  states. The corresponding lattice irreps  $G_1$  and  $H$  are faithful representations of these continuum spins, and hence form the basis of the constructions of higher spins. The numbers of operators with up to two derivatives are shown in Table IX. The number of operators classified according to total spin  $J$

$\Sigma$	$\frac{SU(3)}{SU(2)}$	$N_{\text{nonrel}}$	$N_{\text{rel}}$		
S	(10, 4)	1	1	$\phi_S \chi_S$	
	(10, 2)		1	$\phi_S \chi_S$	
	(8, 4)		1	$\frac{1}{\sqrt{2}}(\phi_{MS} \chi_{MS} + \phi_{MA} \chi_{MA})$	
	(8, 2)	1	2	$\frac{1}{\sqrt{2}}(\phi_{MS} \chi_{MS} + \phi_{MA} \chi_{MA})$	
	(1, 2)		1	$\phi_A \chi_A$	
M	(10, 4)		1	MS	$\phi_S \chi_{MS}$
	(10, 2)	1	2		$\phi_S \chi_{MS}$
	(8, 4)	1	1		$\phi_{MS} \chi_S$
	(8, 4)		1	$\frac{1}{\sqrt{2}}(-\phi_{MS} \chi_{MS} + \phi_{MA} \chi_{MA})$	
	(8, 2)		1	$\phi_{MS} \chi_S$	
	(8, 2)	1	2	$\frac{1}{\sqrt{2}}(-\phi_{MS} \chi_{MS} + \phi_{MA} \chi_{MA})$	
	(8, 2)		1	$\phi_{MA} \chi_A$	
	(1, 4)		1	$\phi_A \chi_{MA}$	
	(1, 2)	1	2	$\phi_A \chi_{MA}$	
A	(10, 2)		1	MA	$\phi_S \chi_{MA}$
	(8, 4)		1		$\phi_S \chi_{MA}$
	(8, 2)	1	2		$\phi_{MA} \chi_S$
	(8, 2)		1	$\frac{1}{\sqrt{2}}(\phi_{MS} \chi_{MA} + \phi_{MA} \chi_{MS})$	
	(1, 4)		1	$\phi_{MA} \chi_S$	
	(1, 2)		1	$\frac{1}{\sqrt{2}}(\phi_{MS} \chi_{MA} + \phi_{MA} \chi_{MS})$	
A	(10, 2)		1	$\phi_S \chi_A$	
	(8, 4)		1	$\frac{1}{\sqrt{2}}(\phi_{MS} \chi_{MA} - \phi_{MA} \chi_{MS})$	
	(8, 2)	1	2	$\frac{1}{\sqrt{2}}(\phi_{MS} \chi_{MA} - \phi_{MA} \chi_{MS})$	
	(1, 4)	1	1	$\phi_A \chi_S$	
	(1, 2)		1	$\phi_A \chi_S$	

TABLE VIII: Local operators classified according to symmetry of flavor and Dirac spin. The dimensionality of the  $SU(3)$  representation is shown. The number of Dirac spin embeddings (number of operators) in a non-relativistic ( $\rho = +$ ) construction are shown in column  $N_{\text{nonrel}}$ , and the number of constructions featuring some number of lower components is shown in column  $N_{\text{rel}}$ . The total number of embeddings is the sum of  $N_{\text{nonrel}} + N_{\text{rel}}$ . The multiplicity of operators in the non-relativistic case is **56** (S), **70** (MS), **70** (MA) and **20** (A), and corresponds to the conventional non-relativistic  $SU(6) \otimes O(3)$  construction. The relativistic construction, which involves both positive and negative parity operators, corresponds to the reduction of  $SU(12)$ . Note that the flavor singlet operators are distinct from the octet and decuplet operators. In the  $SU(3)$  flavor limit, the flavor singlet states do not mix with the octet or decuplet states.

and irrep are shown in Table A 3. A general feature of the operator construction is that there is always an equal number of positive and negative parity operators. For example, for every operator in  $G_{1g}$ , there is a corresponding operator in  $G_{1u}$  and similarly for  $H_g$  and  $H_u$ . There are no single-site operators in  $G_2$ .

These constructions provide operators that have good total angular momentum up to  $J = \frac{7}{2}$  in the continuum limit. However, they are reducible with respect to the octahedral group that represents the symmetry of a cubic lattice.

## Appendix B: Quantum mechanics of continuum spin in the octahedral representation

In this appendix we develop the subduction of  $SU(2)$  quantum states to irreducible octahedral states in the continuum. The lowest spins are trivial as suitable subductions for spins  $J = \frac{1}{2}$  and  $J = \frac{3}{2}$  are provided by the

elementary  $G_1$  and  $H$  octahedral irrep states, i.e.,

$$\begin{aligned} \left| \left[ \frac{1}{2}, m \right] \right\rangle &= \left| G_1, r, \left[ \frac{1}{2} \right] \right\rangle, \quad r = \frac{3}{2} - m, \\ \left| \left[ \frac{3}{2}, m \right] \right\rangle &= \left| H, r, \left[ \frac{3}{2} \right] \right\rangle, \quad r = \frac{5}{2} - m. \end{aligned} \quad (\text{B1})$$

A suitable subduction for spin 1 also is trivial in terms of octahedral irrep  $T_1$ ,

$$|[1, m]\rangle = |T_1, r, [1]\rangle, \quad r = 2 - m.$$

Here and in the following we label octahedral states that carry continuum quantum numbers  $J, M$  by placing the quantum numbers in brackets, i.e.,  $|[J, M]\rangle$ . The angular momentum basis states are orthogonal in the continuum and consequently the octahedral states labelled as  $|[J, M]\rangle$  are orthogonal in the continuum limit as follows,

$$\langle [J, M] | [J', M'] \rangle = \delta_{J, J'} \delta_{M, M'}. \quad (\text{B2})$$

However, they are reducible.

Irreducible octahedral states,  $|\Lambda, r, [J]\rangle$ , that are subduced from a single spin  $J$  are labelled by the octahedral irrep,  $\Lambda$ , row  $r$ , and spin  $[J]$  in brackets. Examples

Singlet, <b>1</b>				
IR	$d = 0$	$d = 1$	$d = 2$	Total
$G_1$	1	4	9	14
$H$	0	5	17	22
$G_2$	0	1	8	9
Octet, <b>8</b>				
IR	$d = 0$	$d = 1$	$d = 2$	Total
$G_1$	3	8	17	28
$H$	1	11	36	48
$G_2$	0	3	17	20
Decuplet, <b>10</b>				
IR	$d = 0$	$d = 1$	$d = 2$	Total
$G_1$	1	4	10	15
$H$	2	5	19	26
$G_2$	0	1	10	11

TABLE IX: Numbers of singlet, octet and decuplet operators for each parity according to the irrep and the number of derivatives,  $d$ . Total derivative constructions have been removed.

Singlet, <b>1</b>					
Rep	$J = \frac{1}{2}$	$J = \frac{3}{2}$	$J = \frac{5}{2}$	$J = \frac{7}{2}$	Total
$G_1$	13			1	14
$H$		13	8	1	22
$G_2$			8	1	9
Octet, <b>8</b>					
Rep	$J = \frac{1}{2}$	$J = \frac{3}{2}$	$J = \frac{5}{2}$	$J = \frac{7}{2}$	Total
$G_1$	24			4	28
$H$		28	16	4	48
$G_2$			16	4	20
Decuplet, <b>10</b>					
Rep	$J = \frac{1}{2}$	$J = \frac{3}{2}$	$J = \frac{5}{2}$	$J = \frac{7}{2}$	Total
$G_1$	12			3	15
$H$		15	8	3	26
$G_2$			8	3	11

TABLE X: Number of singlet, octet and decuplet operators according to continuum spin and subduced irrep. With two derivatives, at most  $J = \frac{7}{2}$  can be reached.

appear on the right side of Eq. (B1). Owing to the orthogonality of different octahedral irreps and rows, these states form an orthonormal set obeying,

$$\langle \Lambda, r, [J] | \Lambda', r', [J] \rangle = \delta_{\Lambda, \Lambda'} \delta_{r, r'}. \quad (\text{B3})$$

A general octahedral irrep can contain an infinite number of continuum spins. States transforming as the same octahedral irrep and row but subduced from different spins, such as  $|H, r, [\frac{3}{2}]\rangle$ ,  $|H, r, [\frac{5}{2}]\rangle$  and  $|H, r, [\frac{7}{2}]\rangle$ , are distinguished by their  $[J]$  labels. These states are orthogonal to

one another as shown in Eq. (B11). The lowest spins have a one-to-one relation between the  $|[J, M]\rangle$  and  $|\Lambda, r, [J]\rangle$  labellings as in Eq. (B1) but higher spins do not.

Higher-spin states can be constructed from direct products of lower-spin states by use of the  $SU(2)$  Clebsch-Gordan formula for direct products of states of spins  $J_1$  and  $J_2$  as follows,

$$|[J, M]\rangle = \sum_{m_1, m_2} |[J_1, m_1]\rangle \otimes |[J_2, m_2]\rangle \times \langle J_1 m_1; J_2 m_2 | JM \rangle, \quad (\text{B4})$$

where  $\langle J_1 m_1; J_2 m_2 | JM \rangle$  is a  $SU(2)$  Clebsch-Gordan coefficient. Equation (B4) provides a block-diagonal unitary transformation between the basis of  $(2J_1+1)(2J_2+1)$  product states on the right side and the equal number of states in the basis of total angular momentum on the left side for  $J$  in the range  $|J_1 - J_2| \leq J \leq J_1 + J_2$ .

Each of the octahedral states should be expanded in terms of a set of  $(2J_1+1)(2J_2+1)$  linearly independent states transforming as irreducible representations of the octahedral group and subduced from a single  $J$  value. Tables XI and XII show the relevant states based on using  $J_1 = 1$  and  $J_2 = \frac{3}{2}$  or  $\frac{5}{2}$  to construct  $J = \frac{5}{2}$  or  $J = \frac{7}{2}$ .

The limited dimensions of the octahedral irreps require multiple occurrences of some irreps in the subduction of high spins. In the continuum, the different occurrences of the same irrep and row provide linearly independent states, as we will show by construction. Representations with multiple occurrences are denoted as  $|^n \Lambda, r, [J]\rangle$ , where  $^n \Lambda$  denotes the  $n^{\text{th}}$  occurrence of irrep  $\Lambda$ ,  $r$  denotes the row of the irrep and  $[J]$  shows the spin from which the state is subduced. When there is a single occurrence, the left superscript is omitted.

Expanding in terms of a complete set of irreducible octahedral states gives,

$$\begin{aligned} |[J, M]\rangle &= \sum_{^n \Lambda, r} |^n \Lambda, r, [J]\rangle \langle ^n \Lambda, r, [J] | [J, M] \rangle, \\ &= \sum_{^n \Lambda, r} |^n \Lambda, r, [J]\rangle \mathcal{S}_{^n \Lambda, r}^{J, M}, \\ \mathcal{S}_{^n \Lambda, r}^{J, M} &= \langle ^n \Lambda, r, [J] | [J, M] \rangle, \end{aligned} \quad (\text{B5})$$

where we sum over all irreps, including multiple occurrences of the same irrep, that are linearly independent. The subduction matrix,  $\mathcal{S}_{^n \Lambda, r}^{J, M}$ , is defined by the overlap of an irreducible octahedral state subduced from a single  $J$  and the spin state  $|[J, M]\rangle$ . Orthogonality properties of the subduction matrices follow from substituting Eq. (B5) into Eq. (B2) with  $J = J'$  as follows,

$$\sum_{\Lambda, r} \sum_{\Lambda', r'} \mathcal{S}_{\Lambda, r}^{J, M} \mathcal{S}_{\Lambda', r'}^{J, M'} \langle \Lambda, r, [J] | \Lambda', r', [J] \rangle = \delta_{M, M'}. \quad (\text{B6})$$

Because of Eq. (B3), this reduces to

$$\sum_{\Lambda, r} \mathcal{S}_{\Lambda, r}^{J, M} \mathcal{S}_{\Lambda, r}^{J, M'} = \delta_{M, M'}. \quad (\text{B7})$$



$J$	$\frac{1}{2}$	$\frac{3}{2}$	$\frac{5}{2}$
IR states	$ G_1, r, [\frac{1}{2}]\rangle$	$ H, r, [\frac{3}{2}]\rangle$	$ H, r, [\frac{5}{2}]\rangle,  G_2, r, [\frac{5}{2}]\rangle$

TABLE XI: Occurrences of octahedral irrep states with spins  $J = \frac{1}{2}$ ,  $\frac{3}{2}$  and  $\frac{5}{2}$  based on using  $J_1 = 1$  and  $J_2 = \frac{3}{2}$ .

$J$	$\frac{3}{2}$	$\frac{5}{2}$	$\frac{7}{2}$
IR states	$ H, r, [\frac{3}{2}]\rangle$	$ H, r, [\frac{5}{2}]\rangle,  G_2, r, [\frac{5}{2}]\rangle$	$ G_1, r, [\frac{7}{2}]\rangle,  H, r, [\frac{7}{2}]\rangle,  G_2, r, [\frac{7}{2}]\rangle$

TABLE XII: Occurrences of octahedral irrep states with spins  $J = \frac{3}{2}$ ,  $\frac{5}{2}$  and  $\frac{7}{2}$  based on  $J_1 = 1$  and  $J_2 = \frac{5}{2}$ .

Summation of the squares of  $\mathcal{S}_{\Lambda, r}^{J, M}$  over  $\Lambda$  and  $r$  gives the normalization condition,

$$\sum_{\Lambda, r} \mathcal{S}_{\Lambda, r}^{J, M} \mathcal{S}_{\Lambda, r}^{J, M} = 1. \quad (\text{B8})$$

Because the  $|[J, M]\rangle$  states are a complete set over the subspace of spin  $J$ , there is a sum rule

$$\begin{aligned} \sum_M \langle \Lambda, r, [J] | [J, M] \rangle \langle [J, M] | \Lambda', r', [J] \rangle \\ = \langle \Lambda, r, [J] | \Lambda', r', [J] \rangle. \end{aligned}$$

where  $\sum_M |[J, M]\rangle \langle [J, M]| = 1$  was used to obtain the right side. The left side involves a sum over products of subduction matrices and the right side involves the  $\delta$ -functions of Eq. (B3), yielding

$$\sum_M \mathcal{S}_{\Lambda, r}^{J, M} \mathcal{S}_{\Lambda', r'}^{J, M} = \delta_{\Lambda, \Lambda'} \delta_{r, r'}. \quad (\text{B9})$$

Multiplying a subduction matrix times both sides of Eq. (B5) and summing over  $M$  yields

$$\begin{aligned} \sum_M \mathcal{S}_{\Lambda, r}^{J, M} |[J, M]\rangle &= \sum_M \mathcal{S}_{\Lambda, r}^{J, M} \sum_{\Lambda', r'} \mathcal{S}_{\Lambda', r'}^{J, M} |\Lambda', r', [J]\rangle \\ &= |\Lambda, r, [J]\rangle, \end{aligned} \quad (\text{B10})$$

where Eq. (B9) was used to evaluate the summations on the right side. This last equation shows how the subduction matrix is used. Once one has a realization of  $|[J, M]\rangle$  states, the subduction matrix is applied to obtain the octahedral irrep states that are subduced from a single  $J$  value. Using Eq. (B10) leads to an important extension of Eq. (B3),

$$\begin{aligned} \langle \Lambda, r, [J] | \Lambda', r', [J'] \rangle &= \sum_{M, M'} \mathcal{S}_{\Lambda, r}^{J, M} \langle [J, M] | [J', M'] \rangle \mathcal{S}_{\Lambda', r'}^{J', M'} \\ &= \sum_{M, M'} \mathcal{S}_{\Lambda, r}^{J, M} \delta_{J, J'} \delta_{M, M'} \mathcal{S}_{\Lambda', r'}^{J', M'} \\ &= \sum_M \mathcal{S}_{\Lambda, r}^{J, M} \mathcal{S}_{\Lambda', r'}^{J, M} \delta_{J, J'} \\ &= \delta_{\Lambda, \Lambda'} \delta_{r, r'} \delta_{J, J'}, \end{aligned} \quad (\text{B11})$$

where Eq. (B9) was used in the last step. The octahedral states subduced from single  $J$  values are orthonormal

with respect to  $J$  as well as with respect to octahedral irrep,  $\Lambda$ , and row,  $r$ .

Substituting the expansion in terms of orthonormal irrep states for each octahedral state in the Clebsch-Gordan formula of Eq. (B4) gives

$$\begin{aligned} \sum_{n\Lambda, r} |^n\Lambda, r, [J]\rangle \mathcal{S}_{n\Lambda, r}^{J, M} &= \sum_{\substack{m_1, m_2 \\ \Lambda_1, r_1 \\ \Lambda_2, r_2}} |\Lambda_1, r_1, [J_1]\rangle \otimes |\Lambda_2, r_2, [J_2]\rangle \\ &\quad \times \mathcal{S}_{\Lambda_1, r_1}^{J_1, m_1} \mathcal{S}_{\Lambda_2, r_2}^{J_2, m_2} \langle J_1 m_1; J_2 m_2 | JM \rangle \end{aligned} \quad (\text{B12})$$

Here the octahedral irrep states on the right side are assumed not to involve multiple occurrences so left superscripts are omitted for  $\Lambda_1$  and  $\Lambda_2$ .

The rules for combining direct products of octahedral group irreps are similar to those for continuum spins. The direct product  $T_1 \otimes H$  corresponds to a direct product of  $J = 1$  and  $J = \frac{3}{2}$  continuum irreps. It yields a  $G_1$  irrep that corresponds to spin- $\frac{1}{2}$ , a  $H$  irrep that corresponds to spin- $\frac{3}{2}$  and a pair of irreps,  $H'$  and  $G_2$ , that taken together correspond to spin- $[\frac{5}{2}]$ . The  $H$  and  $H'$  irrep states are orthogonal in the continuum limit because they are subduced from different spins, i.e.,  $J = \frac{3}{2}$  and  $\frac{5}{2}$ .

Direct products of octahedral states are equal to sums of irreducible states according to the Clebsch-Gordan formula for the octahedral group,

$$\begin{aligned} |\Lambda_1, r_1, [J_1]\rangle \otimes |\Lambda_2, r_2, [J_2]\rangle &= \sum_{\Lambda_{\Lambda_1 \otimes \Lambda_2}, r} |\Lambda_{\Lambda_1 \otimes \Lambda_2}, r\rangle \cdot C \begin{pmatrix} \Lambda_1 & \Lambda_2 & \Lambda_{\Lambda_1 \otimes \Lambda_2} \\ r_1 & r_2 & r \end{pmatrix}, \end{aligned} \quad (\text{B13})$$

where the states produced on the right side are labeled by the irreps involved in the direct products. The  $[J_1]$  and  $[J_2]$  labels of the states on the left side are passive and do not affect the direct products. This gives the following expansion,

$$\sum_{n\Lambda, r} |^n\Lambda, r, [J]\rangle \mathcal{S}_{n\Lambda, r}^{J, M} = \sum_{\Lambda_{\Lambda_1 \otimes \Lambda_2}, r} |\Lambda_{\Lambda_1 \otimes \Lambda_2}, r\rangle \mathcal{R}_{\Lambda_{\Lambda_1 \otimes \Lambda_2}, r}^{J, M}, \quad (\text{B14})$$

$J$	$\frac{5}{2}$	$\frac{7}{2}$	$\frac{9}{2}$
IR states	$ H, r, [\frac{5}{2}]\rangle,  G_2, r, [\frac{5}{2}]\rangle$	$ G_1, r, [\frac{7}{2}]\rangle,  H, r, [\frac{7}{2}]\rangle,  G_2, r, [\frac{7}{2}]\rangle$	$ G_1, r, [\frac{9}{2}]\rangle,  ^1H, r, [\frac{9}{2}]\rangle,  ^2H, r, [\frac{9}{2}]\rangle$

TABLE XIII: Occurrences of octahedral irrep states in the subduction of spin  $\frac{9}{2}$  based on  $J_1 = 1$  and  $J_2 = \frac{7}{2}$ 

where matrix  $\mathcal{R}_{\Lambda_{\Lambda_1 \otimes \Lambda_2}, r}^{J, M}$  is defined by

$$\begin{aligned} \mathcal{R}_{\Lambda_{\Lambda_1 \otimes \Lambda_2}, r}^{J, M} = & \sum_{\substack{m_1, m_2 \\ \Lambda_1, r_1 \\ \Lambda_2, r_2}} C \begin{pmatrix} \Lambda_1 & \Lambda_2 & \Lambda_{\Lambda_1 \otimes \Lambda_2} \\ r_1 & r_2 & r \end{pmatrix} \\ & \times \mathcal{S}_{\Lambda_1, r_1}^{J_1, m_1} \mathcal{S}_{\Lambda_2, r_2}^{J_2, m_2} \\ & \times \langle J_1 m_1; J_2 m_2 | JM \rangle. \end{aligned} \quad (\text{B15})$$

The notation used here is based on the fact that the states produced by the Clebsch-Gordan expansion are general octahedral irrep states, not states subduced from a single  $J$  value. For the construction based on Eq. (B12), the  $SU(2)$  spins in the range  $|J_1 - J_2| \leq J \leq J_1 + J_2$  provide a complete set of  $(2J_1 + 1)(2J_2 + 1)$  linearly independent states and the octahedral irrep states on the right side of Eq. (B14) can be expanded as a linear combination of the octahedral irrep states subduced from a single spin as follows,

$$|\Lambda_{\Lambda_1 \otimes \Lambda_2}, r\rangle = \sum_{J'=|J_1-J_2|}^{J_1+J_2} \mathcal{A}_{\Lambda_{\Lambda_1 \otimes \Lambda_2}, n\Lambda[J']} |^n\Lambda, r, [J']\rangle \quad (\text{B16})$$

where  $\mathcal{A}_{\Lambda_{\Lambda_1 \otimes \Lambda_2}, n\Lambda[J']}$  is a matrix in the  $\Lambda_{\Lambda_1 \otimes \Lambda_2}$  and  $n\Lambda[J]$  indices.

Substituting Eqs. (B13) and (B16) into Eq. (B12) and using Eq. (B5) gives

$$\begin{aligned} \sum_{n\Lambda, r} |^n\Lambda, r, [J]\rangle \mathcal{S}_{n\Lambda, r}^{J, M} = & \sum_{J', \Lambda_{\Lambda_1 \otimes \Lambda_2}, r} \mathcal{A}_{\Lambda_{\Lambda_1 \otimes \Lambda_2}, n\Lambda[J']} \\ & \times |^n\Lambda, r, [J']\rangle \mathcal{R}_{\Lambda_{\Lambda_1 \otimes \Lambda_2}, r}^{J, M} \end{aligned} \quad (\text{B17})$$

Because the octahedral states  $|^n\Lambda, r, [J]\rangle$  that are subduced from a single spin form an orthonormal set, their coefficients must be the same on both sides of Eq. (B17). Thus, the subduction matrix for total spin,  $J$ , obeys

$$\mathcal{S}_{n\Lambda, r}^{J, M} = \sum_{\Lambda_{\Lambda_1 \otimes \Lambda_2}} \mathcal{A}_{\Lambda_{\Lambda_1 \otimes \Lambda_2}, n\Lambda[J]} \mathcal{R}_{\Lambda_{\Lambda_1 \otimes \Lambda_2}, r}^{J, M} \quad (\text{B18})$$

As will become evident, matrix  $\mathcal{A}$  is orthogonal:  $\mathcal{A}\mathcal{A}^T = 1$ . When the above equation is multiplied by  $|[J, M]\rangle$  on both sides, and then summed over  $M$ , we get

$$\begin{aligned} \sum_M \mathcal{S}_{n\Lambda, r}^{J, M} |[J, M]\rangle = & \sum_{\Lambda_{\Lambda_1 \otimes \Lambda_2}} \mathcal{A}_{\Lambda_{\Lambda_1 \otimes \Lambda_2}, n\Lambda[J]} \\ & \times \sum_M \mathcal{R}_{\Lambda_{\Lambda_1 \otimes \Lambda_2}, r}^{J, M} |[J, M]\rangle \end{aligned} \quad (\text{B19})$$

Using Eq. (B5), this becomes

$$|^n\Lambda, r, [J]\rangle = \sum_{\Lambda_{\Lambda_1 \otimes \Lambda_2}} \mathcal{A}_{\Lambda_{\Lambda_1 \otimes \Lambda_2}, n\Lambda[J]} |\Lambda_{\Lambda_1 \otimes \Lambda_2}, r\rangle, \quad (\text{B20})$$

where

$$|\Lambda_{\Lambda_1 \otimes \Lambda_2}, r\rangle = \sum_M \mathcal{R}_{\Lambda_{\Lambda_1 \otimes \Lambda_2}, r}^{J, M} |[J, M]\rangle. \quad (\text{B21})$$

Table XIV shows the subduction matrices for the elementary states of spin  $\frac{1}{2}$ , 1 and  $\frac{3}{2}$ . They are unit matrices in the basis used. Starting with the known subduction matrices for spins  $J_1 = 1$  and  $J_2 = \frac{3}{2}$ , the subduction matrix for spin  $\frac{5}{2}$  can be obtained as follows. Evaluate Eq. (B15) to obtain matrices  $\mathcal{R}_{H'_{T_1 \otimes H}, r}^{\frac{5}{2}, M}$ ,  $\mathcal{R}_{H_{T_1 \otimes H}, r}^{\frac{3}{2}, M}$  and  $\mathcal{R}_{G_2 T_1 \otimes H, r}^{\frac{5}{2}, M}$ . Matrix  $\mathcal{R}_{H'_{T_1 \otimes H}, r}^{\frac{5}{2}, M}$  is equal within an overall constant factor  $\mathcal{A}_{H'[\frac{5}{2}], H_{T_1 \otimes H}}$  to subduction matrix  $\mathcal{S}_{H, r}^{\frac{5}{2}, M}$ . Similarly,  $\mathcal{R}_{H_{T_1 \otimes H}, r}^{\frac{3}{2}, M}$  and  $\mathcal{R}_{G_2 T_1 \otimes H, r}^{\frac{5}{2}, M}$  are equal within overall factors to  $\mathcal{S}_{H, r}^{\frac{3}{2}, M}$  and  $\mathcal{S}_{G_2, r}^{\frac{5}{2}, M}$ . The overall factors lead to  $\mathcal{S}$  matrices normalized as in Eq. (B8). The subduction matrices that are obtained for spin  $\frac{5}{2}$  are given in Table XV. The overall factors determine matrix  $\mathcal{A}_{n\Lambda[J], \Lambda_{\Lambda_1 \otimes \Lambda_2}}$ , which is a unit matrix in this example, i.e., Eq. (B16) takes the form,

$$\begin{pmatrix} |H_{T_1 \otimes H}, r\rangle \\ |H'_{T_1 \otimes H}, r\rangle \\ |G_2 T_1 \otimes H, r\rangle \end{pmatrix} = \begin{pmatrix} 1 & 0 & 0 \\ 0 & 1 & 0 \\ 0 & 0 & 1 \end{pmatrix} \begin{pmatrix} |H, r, [\frac{3}{2}]\rangle \\ |H, r, [\frac{5}{2}]\rangle \\ |G_2, r, [\frac{5}{2}]\rangle \end{pmatrix}. \quad (\text{B22})$$

This block-matrix equation holds when the row indices,  $r$ , are the same on both sides. Note that orthonormality of the states on the right side implies that the states on the left side are orthonormal.

For higher spins, the Clebsch-Gordan coefficients of the octahedral group do not provide a block-diagonal result for the subduction, i.e., matrix  $\mathcal{A}$  takes a non-trivial form. This is demonstrated for the construction of spin  $\frac{7}{2}$  based on  $J_1 = 1$  and  $J_2 = \frac{5}{2}$ , which involves use of the previous subduction,  $[\frac{5}{2}] \rightarrow H \oplus G_2$ . Three orthogonal occurrences of irrep  $H$  are produced in the  $T_1 \otimes [\frac{5}{2}] = T_1 \otimes (H \oplus G_2)$  direct products and two orthogonal occurrences of  $G_2$  are produced. Taking into account the fact that two different  $H$  irreps are produced by each  $T_1 \otimes H$  product, i.e.,  $T_1 \otimes H \rightarrow G_1 \oplus H \oplus H' \oplus G_2$ , the three  $H$  states that occur are  $H_{T_1 \otimes H}$ ,  $H'_{T_1 \otimes H}$  and  $H_{T_1 \otimes G_2}$ .

The two different  $G_2$  states that occur are  $G_2 T_1 \otimes H$  and  $G_2 T_1 \otimes G_2$ .

The procedure is similar to the spin  $\frac{5}{2}$  case. First one evaluates Eq. (B15) to obtain matrices  $\mathcal{R}_{G_1 T_1 \otimes H, r}^{\frac{7}{2}, M}$ ,  $\mathcal{R}_{H T_1 \otimes H, r}^{\frac{7}{2}, M}$ ,  $\mathcal{R}_{H' T_1 \otimes H, r}^{\frac{5}{2}, M}$ ,  $\mathcal{R}_{H T_1 \otimes H, r}^{\frac{3}{2}, M}$ ,  $\mathcal{R}_{G_2 T_1 \otimes H, r}^{\frac{7}{2}, M}$  and  $\mathcal{R}_{G_2 T_1 \otimes G_2, r}^{\frac{5}{2}, M}$ . Each  $\mathcal{R}$  matrix corresponds to a single  $\mathcal{S}$  matrix of the set  $\mathcal{S}_{G_1, r}^{\frac{7}{2}, M}$ ,  $\mathcal{S}_{H, r}^{\frac{7}{2}, M}$ ,  $\mathcal{S}_{H', r}^{\frac{5}{2}, M}$ ,  $\mathcal{S}_{H, r}^{\frac{3}{2}, M}$ ,  $\mathcal{S}_{G_2, r}^{\frac{7}{2}, M}$  and  $\mathcal{S}_{G_2, r}^{\frac{5}{2}, M}$ . In this case the subduction matrices for spin  $\frac{7}{2}$  can be obtained simply by imposing the normalization condition  $\sum_M \mathcal{S}_{\Lambda, r}^{J, M} \mathcal{S}_{\Lambda, r}^{J, M} = 1$ . That gives the subduction matrices of Table XVI.

The octahedral states that result from the Clebsch-Gordan formula are linear combinations of the states subduced from a single  $J$  value. This is expressed by the block-matrix equation,

$$\begin{pmatrix} |G_1 T_1 \otimes H, r\rangle \\ |H T_1 \otimes H, r\rangle \\ |H' T_1 \otimes H, r\rangle \\ |H T_1 \otimes G_2, r\rangle \\ |G_2 T_1 \otimes H, r\rangle \\ |G_2 T_1 \otimes G_2, r\rangle \end{pmatrix} = \mathcal{A}^{T_1 \otimes \frac{5}{2}} \times \begin{pmatrix} |G_1, r, [\frac{7}{2}]\rangle \\ |H, r, [\frac{7}{2}]\rangle \\ |H, r, [\frac{5}{2}]\rangle \\ |H, r, [\frac{3}{2}]\rangle \\ |G_2, r, [\frac{7}{2}]\rangle \\ |G_2, r, [\frac{5}{2}]\rangle \end{pmatrix}. \quad (\text{B23})$$

where matrix  $\mathcal{A}^{T_1 \otimes \frac{5}{2}}$  is

$$\mathcal{A}^{T_1 \otimes \frac{5}{2}} = \begin{pmatrix} 1 & 0 & 0 & 0 & 0 & 0 \\ 0 & \sqrt{\frac{4}{7}} & \sqrt{\frac{3}{7}} & 0 & 0 & 0 \\ 0 & -\sqrt{\frac{1}{7}} & \sqrt{\frac{4}{21}} & -\sqrt{\frac{2}{3}} & 0 & 0 \\ 0 & -\sqrt{\frac{2}{7}} & \sqrt{\frac{8}{21}} & \sqrt{\frac{1}{3}} & 0 & 0 \\ 0 & 0 & 0 & 0 & \sqrt{\frac{5}{21}} & -\sqrt{\frac{16}{21}} \\ 0 & 0 & 0 & 0 & -\sqrt{\frac{16}{21}} & -\sqrt{\frac{5}{21}} \end{pmatrix}. \quad (\text{B24})$$

Note that row indices,  $r$ , are the same on both sides of Eq. (B23) so that it connects the 18 states on the left side (considering all allowed values of the row indices) to 18 states on the right side. The states on the right side are orthonormal as in Eq. (B11) and the rows of the matrix in Eq. (B23) are orthogonal to one another. It follows that the states on the left side also form an orthonormal set by construction. Matrix equation (B23) takes the form of Eq. (B16) and it provides a nontrivial example of matrix  $\mathcal{A}$ , demonstrating the relation between irreducible states resulting from direct products of octahedral states and the irreducible states that are subduced from a single spin. It is straightforward to solve for the irreducible states subduced from a single spin by applying  $\mathcal{A}^{-1} = \mathcal{A}^T$  to both sides of Eq. (B23). That demonstrates that the irreducible octahedral states subduced from a single  $J$  are linear combinations of the irreducible octahedral states resulting from the Clebsch-Gordan formula.

The same reasoning can be applied to the subduction of spin  $\frac{9}{2}$  based on  $J_1 = 1$  and  $J_2 = \frac{7}{2}$ . Table XIII

shows the linearly independent states for this case. A total of four orthogonal occurrences of  $H$ , two of  $G_1$  and two of  $G_2$  arise from  $T_1 \otimes [\frac{7}{2}] = T_1 \otimes (G_1 \oplus H \oplus G_2)$ . Two of the  $H$  irreps reproduce the previous results for subduction of spins  $\frac{5}{2}$  and  $\frac{7}{2}$ . The other two  $H$  irreps are yet-to-be-determined subductions of spin  $\frac{9}{2}$ . The two  $G_1$  irreps provide subductions of spins  $\frac{9}{2}$  and  $\frac{7}{2}$ . The two  $G_2$  irreps provide subductions of spins  $\frac{7}{2}$  and  $\frac{5}{2}$ . The new element for spin  $\frac{9}{2}$  is that two occurrences of irrep  $H$  are unknown. They are determined as follows. First matrices  $\mathcal{R}_{\Lambda_1 \otimes \Lambda_2, r}^{J, M}$  are calculated. They are related to the subduction matrices by a matrix  $\mathcal{A}^{T_1 \otimes \frac{7}{2}}$ , which also relates the states formed from the  $\mathcal{R}$  and  $\mathcal{S}$  matrices as in Eqs. (B10) and (B21). That relation can be expressed as follows,

$$\begin{pmatrix} |G_1 T_1 \otimes G_1, r\rangle \\ |G_1 T_1 \otimes H, r\rangle \\ |H_1 T_1 \otimes G_1, r\rangle \\ |H T_1 \otimes H, r\rangle \\ |H' T_1 \otimes H, r\rangle \\ |H T_1 \otimes G_2, r\rangle \\ |G_2 T_1 \otimes H, r\rangle \\ |G_2 T_1 \otimes G_2, r\rangle \end{pmatrix} = \mathcal{A}^{T_1 \otimes \frac{7}{2}} \times \begin{pmatrix} |G_1, r, [\frac{9}{2}]\rangle \\ |G_1, r, [\frac{7}{2}]\rangle \\ |^1 H, r, [\frac{9}{2}]\rangle \\ |^2 H, r, [\frac{9}{2}]\rangle \\ |H, r, [\frac{7}{2}]\rangle \\ |H, r, [\frac{5}{2}]\rangle \\ |G_2, r, [\frac{7}{2}]\rangle \\ |G_2, r, [\frac{5}{2}]\rangle \end{pmatrix}. \quad (\text{B25})$$

where matrix  $\mathcal{A}^{T_1 \otimes \frac{7}{2}}$  is

$$\begin{pmatrix} \sqrt{\frac{20}{27}} & -\sqrt{\frac{7}{27}} & 0 & 0 & 0 & 0 & 0 & 0 \\ -\sqrt{\frac{7}{27}} & -\sqrt{\frac{20}{27}} & 0 & 0 & 0 & 0 & 0 & 0 \\ 0 & 0 & a_1 & b_1 & \sqrt{\frac{10}{27}} & \sqrt{\frac{3}{8}} & 0 & 0 \\ 0 & 0 & a_2 & b_2 & \sqrt{\frac{1}{945}} & -\sqrt{\frac{3}{7}} & 0 & 0 \\ 0 & 0 & a_3 & b_3 & -\sqrt{\frac{12}{35}} & \sqrt{\frac{3}{28}} & 0 & 0 \\ 0 & 0 & a_4 & b_4 & -\sqrt{\frac{2}{7}} & \sqrt{\frac{5}{56}} & 0 & 0 \\ 0 & 0 & 0 & 0 & 0 & 0 & \sqrt{\frac{4}{7}} & -\sqrt{\frac{3}{7}} \\ 0 & 0 & 0 & 0 & 0 & 0 & \sqrt{\frac{3}{7}} & \sqrt{\frac{4}{7}} \end{pmatrix}. \quad (\text{B26})$$

Constants  $a_n$  and  $b_n$  express the unknown parts of the matrix that connect the four  $H$  irreps on the left side to linear combinations involving  $|^1 H, r, [\frac{9}{2}]\rangle$  and  $|^2 H, r, [\frac{9}{2}]\rangle$ .

The upper-left block of the matrix equation can be solved for

$$|G_1, r, [\frac{9}{2}]\rangle = \sqrt{\frac{20}{27}} |G_1 T_1 \otimes G_1, r\rangle - \sqrt{\frac{7}{27}} |G_1 T_1 \otimes H, r\rangle. \quad (\text{B27})$$

Subduction matrix  $\mathcal{S}_{G_1, r}^{\frac{9}{2}, M}$  is determined by a linear combination of  $\mathcal{R}$  matrices with the same coefficients as in

Eq. (B27), i.e.,

$$\mathcal{S}_{G_1,r}^{\frac{9}{2},M} = \sqrt{\frac{20}{27}} \mathcal{R}_{G_1 T_1 \otimes G_1,r}^{\frac{9}{2},M} - \sqrt{\frac{7}{27}} \mathcal{R}_{G_1 T_1 \otimes H,r}^{\frac{9}{2},M}. \quad (\text{B28})$$

The middle block gives four equations for the  $H$  irreps. They can be reduced to three by making linear combinations of pairs of equations to eliminate the  $|H, r, [\frac{5}{2}]\rangle$  terms, and then further reduced to two equations by making linear combinations of pairs of equations to eliminate the  $|H, r, [\frac{7}{2}]\rangle$  terms. The resulting equations provide candidates for the  ${}^1H$  and  ${}^2H$  irrep states subduced from spin  $\frac{9}{2}$  as follows,

$$a_1'' |{}^1H, r, [\frac{9}{2}]\rangle + b_1'' |{}^2H, r, [\frac{9}{2}]\rangle = \sqrt{\frac{5}{96}} |H_{T_1 \otimes G_1}, r\rangle + \sqrt{\frac{7}{60}} |H_{T_1 \otimes H}, r\rangle + \sqrt{\frac{21}{320}} |H'_{T_1 \otimes H}, r\rangle$$

$$a_2'' |{}^1H, r, [\frac{9}{2}]\rangle + b_2'' |{}^2H, r, [\frac{9}{2}]\rangle = \frac{5}{24} |H_{T_1 \otimes G_1}, r\rangle + \sqrt{\frac{7}{72}} |H_{T_1 \otimes H}, r\rangle - \sqrt{\frac{21}{320}} |H_{T_1 \otimes G_2}, r\rangle,$$

where  $a_n''$  and  $b_n''$  are combinations of the unknown constants  $a_n$  and  $b_n$ . There remain four unknown constants here and three equations that constrain them in order that states  $|{}^1H, r, [\frac{9}{2}]\rangle$  and  $|{}^2H, r, [\frac{9}{2}]\rangle$  are orthonormal. A one-parameter family of solutions exists. It is sufficient for our purpose to obtain a single solution by choosing  $b_1'' = 0$ . From the first equation we find

$$|{}^1H, r, [\frac{9}{2}]\rangle = \sqrt{\frac{2}{9}} |H_{T_1 \otimes G_1}, r\rangle + \sqrt{\frac{112}{225}} |H_{T_1 \otimes H}, r\rangle + \sqrt{\frac{7}{25}} |H'_{T_1 \otimes H}, r\rangle, \quad (\text{B29})$$

where constant  $a_1''$  was determined by normalizing the state. The second equation is then used to obtain a state that is orthonormal to the first one, which determines constants  $a_2''$  and  $b_2''$ , and yields

$$|{}^2H, r, [\frac{9}{2}]\rangle = \sqrt{\frac{7}{216}} |H_{T_1 \otimes G_1}, r\rangle + \sqrt{\frac{49}{675}} |H_{T_1 \otimes H}, r\rangle - \sqrt{\frac{27}{100}} |H'_{T_1 \otimes H}, r\rangle + \sqrt{\frac{5}{8}} |H_{T_1 \otimes G_2}, r\rangle.$$

The coefficients appearing in Eq. (B29) give the values of  $a_1, a_2, a_3$  ( $a_4 = 0$ ) and the coefficients appearing in

Eq.(B30) give the values of  $b_1, b_2, b_3$  and  $b_4$ . They complete the determination of matrix  $\mathcal{A}$  and can be used to show that it is orthogonal. Subduction matrices are determined as linear combinations of  $\mathcal{R}$  matrices with the same coefficients that appear above for the  ${}^1H$  and  ${}^2H$  states,

$$\begin{aligned} \mathcal{S}_{{}^1H,r}^{\frac{9}{2},M} &= \sqrt{\frac{2}{9}} \mathcal{R}_{H_{T_1 \otimes G_1},r}^{\frac{9}{2},M} + \sqrt{\frac{112}{225}} \mathcal{R}_{H_{T_1 \otimes H},r}^{\frac{9}{2},M} + \sqrt{\frac{7}{25}} \mathcal{R}_{H'_{T_1 \otimes H},r}^{\frac{9}{2},M} \\ \mathcal{S}_{{}^2H,r}^{\frac{9}{2},M} &= \sqrt{\frac{7}{216}} \mathcal{R}_{H_{T_1 \otimes G_1},r}^{\frac{9}{2},M} + \sqrt{\frac{49}{675}} \mathcal{R}_{H_{T_1 \otimes H},r}^{\frac{9}{2},M} - \sqrt{\frac{27}{100}} \mathcal{R}_{H'_{T_1 \otimes H},r}^{\frac{9}{2},M} + \sqrt{\frac{5}{8}} \mathcal{R}_{H_{T_1 \otimes G_2},r}^{\frac{9}{2},M}. \end{aligned} \quad (\text{B30})$$

The resulting subduction matrices for spin  $\frac{9}{2}$  are given in Table XVII.

TABLE XIV: Elementary subduction matrices  $\mathcal{S}_{G_1,r}^{\frac{1}{2},m}$ ,  $\mathcal{S}_{T_1,r}^{1,m}$  and  $\mathcal{S}_{H,r}^{\frac{3}{2},m}$ .

$J = \frac{1}{2} \rightarrow G_1$			$J = 1 \rightarrow T_1$			$J = \frac{3}{2} \rightarrow H$					
$r$	$m$	$+\frac{1}{2} \quad -\frac{1}{2}$	$r$	$m$	$+1 \quad 0 \quad -1$	$r$	$m$	$+\frac{3}{2} \quad +\frac{1}{2} \quad -\frac{1}{2} \quad -\frac{3}{2}$			
1		1   0	1		1   0   0	1		1   0   0   0			
2		0   1	2		0   1   0	2		0   1   0   0			
			3		0   0   1	3		0   0   1   0			
						4		0   0   0   1			

TABLE XV: Subduction matrices  $\mathcal{S}_{H,r}^{\frac{5}{2},m}$  and  $\mathcal{S}_{G_2,r}^{\frac{5}{2},m}$

$J = \frac{5}{2} \rightarrow H$							
$r$	$m$	$+\frac{5}{2}$	$+\frac{3}{2}$	$+\frac{1}{2}$	$-\frac{1}{2}$	$-\frac{3}{2}$	$-\frac{5}{2}$
1		0	$+\sqrt{\frac{1}{6}}$	0	0	0	$+\sqrt{\frac{5}{6}}$
2		0	0	-1	0	0	0
3		0	0	0	+1	0	0
4		$-\sqrt{\frac{5}{6}}$	0	0	0	$-\sqrt{\frac{1}{6}}$	0

$J = \frac{5}{2} \rightarrow G_2$							
$r$	$m$	$+\frac{5}{2}$	$+\frac{3}{2}$	$+\frac{1}{2}$	$-\frac{1}{2}$	$-\frac{3}{2}$	$-\frac{5}{2}$
1		$+\sqrt{\frac{1}{6}}$	0	0	0	$-\sqrt{\frac{5}{6}}$	0
2		0	$-\sqrt{\frac{5}{6}}$	0	0	0	$+\sqrt{\frac{1}{6}}$

TABLE XVI: Subduction matrices  $\mathcal{S}_{G_1,r}^{\frac{7}{2},m}$ ,  $\mathcal{S}_{H,r}^{\frac{7}{2},m}$  and  $\mathcal{S}_{G_2,r}^{\frac{7}{2},m}$ .

$J = \frac{7}{2} \rightarrow G_1$									
$r$	$m$	$+\frac{7}{2}$	$+\frac{5}{2}$	$+\frac{3}{2}$	$+\frac{1}{2}$	$-\frac{1}{2}$	$-\frac{3}{2}$	$-\frac{5}{2}$	$-\frac{7}{2}$
1		0	0	0	$+\sqrt{\frac{7}{12}}$	0	0	0	$+\sqrt{\frac{5}{12}}$
2		$-\sqrt{\frac{5}{12}}$	0	0	0	$-\sqrt{\frac{7}{12}}$	0	0	0

$J = \frac{7}{2} \rightarrow H$									
$r$	$m$	$+\frac{7}{2}$	$+\frac{5}{2}$	$+\frac{3}{2}$	$+\frac{1}{2}$	$-\frac{1}{2}$	$-\frac{3}{2}$	$-\frac{5}{2}$	$-\frac{7}{2}$
1		0	0	$+\sqrt{\frac{3}{4}}$	0	0	0	$+\sqrt{\frac{1}{4}}$	0
2		0	0	0	$-\sqrt{\frac{5}{12}}$	0	0	0	$+\sqrt{\frac{7}{12}}$
3		$+\sqrt{\frac{7}{12}}$	0	0	0	$-\sqrt{\frac{5}{12}}$	0	0	0
4		0	$+\sqrt{\frac{1}{4}}$	0	0	0	$+\sqrt{\frac{3}{4}}$	0	0

$J = \frac{7}{2} \rightarrow G_2$									
$r$	$m$	$+\frac{7}{2}$	$+\frac{5}{2}$	$+\frac{3}{2}$	$+\frac{1}{2}$	$-\frac{1}{2}$	$-\frac{3}{2}$	$-\frac{5}{2}$	$-\frac{7}{2}$
1		0	$+\sqrt{\frac{3}{4}}$	0	0	0	$-\sqrt{\frac{1}{4}}$	0	0
2		0	0	$+\sqrt{\frac{1}{4}}$	0	0	0	$-\sqrt{\frac{3}{4}}$	0

TABLE XVII: Subduction matrices  $\mathcal{S}_{G_1,r}^{\frac{9}{2},m}$ ,  $\mathcal{S}_{H,r}^{\frac{9}{2},m}$  and  $\mathcal{S}_{G_2,r}^{\frac{9}{2},m}$ .

$J = \frac{9}{2} \rightarrow G_1$											
$r$	$m$	$+\frac{9}{2}$	$+\frac{7}{2}$	$+\frac{5}{2}$	$+\frac{3}{2}$	$+\frac{1}{2}$	$-\frac{1}{2}$	$-\frac{3}{2}$	$-\frac{5}{2}$	$-\frac{7}{2}$	$-\frac{9}{2}$
1		$-\sqrt{\frac{3}{8}}$	0	0	0	$-\sqrt{\frac{7}{12}}$	0	0	0	$-\sqrt{\frac{1}{24}}$	0
2		0	$-\sqrt{\frac{1}{24}}$	0	0	0	$-\sqrt{\frac{7}{12}}$	0	0	0	$-\sqrt{\frac{3}{8}}$

$J = \frac{9}{2} \rightarrow {}^1H$											
$r$	$m$	$+\frac{9}{2}$	$+\frac{7}{2}$	$+\frac{5}{2}$	$+\frac{3}{2}$	$+\frac{1}{2}$	$-\frac{1}{2}$	$-\frac{3}{2}$	$-\frac{5}{2}$	$-\frac{7}{2}$	$-\frac{9}{2}$
1		0	0	0	$+\sqrt{\frac{7}{10}}$	0	0	0	$+\sqrt{\frac{3}{10}}$	0	0
2		$-\sqrt{\frac{5}{8}}$	0	0	0	$+\sqrt{\frac{7}{20}}$	0	0	0	$+\sqrt{\frac{1}{40}}$	0
3		0	$-\sqrt{\frac{1}{40}}$	0	0	0	$-\sqrt{\frac{7}{20}}$	0	0	0	$+\sqrt{\frac{5}{8}}$
4		0	0	$-\sqrt{\frac{3}{10}}$	0	0	0	$-\sqrt{\frac{7}{10}}$	0	0	0

$J = \frac{9}{2} \rightarrow {}^2H$											
$r$	$m$	$+\frac{9}{2}$	$+\frac{7}{2}$	$+\frac{5}{2}$	$+\frac{3}{2}$	$+\frac{1}{2}$	$-\frac{1}{2}$	$-\frac{3}{2}$	$-\frac{5}{2}$	$-\frac{7}{2}$	$-\frac{9}{2}$
1		0	0	0	$+\sqrt{\frac{3}{10}}$	0	0	0	$-\sqrt{\frac{7}{10}}$	0	0
2		0	0	0	0	$-\sqrt{\frac{1}{15}}$	0	0	0	$+\sqrt{\frac{14}{15}}$	0
3		0	$-\sqrt{\frac{14}{15}}$	0	0	0	$+\sqrt{\frac{1}{15}}$	0	0	0	0
4		0	0	$+\sqrt{\frac{7}{10}}$	0	0	0	$-\sqrt{\frac{3}{10}}$	0	0	0